

Evaluation of Higher-order Quadrature Schemes in Improving Computational Efficiency for Orientation-averaged Single-Scattering Properties of Nonspherical Ice Particles

Ines FENNI¹, Kwo-Sen Kuo², Mark Haynes³, Ziad S Haddad⁴, and Roussel Hélène⁵

¹UCLA

²National Aeronautics and Space Administration (NASA)

³Jet Propulsion Laboratory

⁴Jet Propulsion Lab (NASA)

⁵Sorbonne University

November 30, 2022

Abstract

We evaluate several high-order quadrature schemes for accuracy and efficacy in obtaining orientation-averaged single-scattering properties (SSPs). We use the recently developed, highly efficient MIDAS to perform electromagnetic scattering calculations to compare and evaluate the gain in efficiency from these quadrature schemes. MIDAS is shown to be superior to DDSCAT, a popular discrete dipole approximation (DDA) method. This study is motivated by the fact that quality physical precipitation retrievals rely on using accurate orientation-averaged SSPs derived from realistic hydrometeors as input to radiative transfer simulations. The DDA has been a popular choice for single-scattering calculations, due to its versatility with respect to target geometry. However, being iterative-solver-based (ISB), the most used DDA codes, e.g. DDSCAT and ADDA, must solve the scattering problem for each orientation of the target separately. As the size parameter and geometric anisotropy of the hydrometeor increase, the number of orientations needed to obtain accurate orientation-averages can increase drastically and so does the computation cost incurred by the ISB-DDA methods. MIDAS is a Direct-Solver-Based (DSB) code, using Method of Moments (MoM) instead of DDA, its decomposition of the original large matrix with a high rank into multiple more manageable smaller matrices of lower ranks makes it much more computationally efficient and stable while maintaining excellent accuracy. In addition, direct solvers consider all requested orientations at once, giving MIDAS further advantage over popular ISB-DDA methods. Combined with high-order quadrature for orientation average, MIDAS can be orders of magnitude more efficient in obtaining RTM-ready SSPs than existing ISB-DDA methods.

Abstract

We evaluate several high-order quadrature schemes for accuracy and efficacy in obtaining orientation-averaged single-scattering properties (SSPs). We use the recently developed, highly efficient MIDAS to perform electromagnetic scattering calculations to compare and evaluate the gain in efficiency from these quadrature schemes. MIDAS is shown to be superior to DDSCAT, a popular discrete dipole approximation (DDA) method. This study is motivated by the fact that quality physical precipitation retrievals rely on using accurate orientation-averaged SSPs derived from realistic hydrometeors as input to radiative transfer simulations. The DDA has been a popular choice for single-scattering calculations, due to its versatility with respect to target geometry. However, being iterative-solver-based (ISB), the most used DDA codes, e.g. DDSCAT and ADDA, must solve the scattering problem for each orientation of the target separately. As the size parameter and geometric anisotropy of the hydrometeor increase, the number of orientations needed to obtain accurate orientation-averages can increase drastically and so does the computation cost incurred by the ISB-DDA methods. MIDAS is a Direct-Solver-Based (DSB) code, using Method of Moments (MoM) instead of DDA, its decomposition of the original large matrix with a high rank into multiple more manageable smaller matrices of lower ranks makes it much more computationally efficient and stable while maintaining excellent accuracy. In addition, direct solvers consider all requested orientations at once, giving MIDAS further advantage over popular ISB-DDA methods. Combined with high-order quadrature for orientation average, MIDAS can be orders of magnitude more efficient in obtaining RTM-ready SSPs than existing ISB-DDA methods.

1 Introduction

Cloud and precipitation warrant extensive and continuous survey because they fundamentally impact the water and energy cycles of our planet, exerting enormous influences on its weather and climate. Spaceborne remote sensing offers a cost-effective means to ensure adequate spatiotemporal observation coverage of these phenomena over unpopulated areas such as the oceans. Thus, the remote sensing of cloud and precipitation has been the focus of multiple NASA Earth Science missions in the past few decades, e.g. the Tropical Rainfall Measuring Mission (TRMM) (Kummerow et al., 1998, 2000), the CloudSat-CALIPSO missions (Stephens et al., 2002, 2008), and the Global Precipitation Measurement (GPM) mission (Hou et al., 2014). Aiming to achieve a better understanding of their impacts, observations of cloud and precipitation from the active and passive microwave instruments of these missions have been extensively and routinely used for monitoring and analyzed to improve their quantitative physical estimates.

The canonical approach in physical precipitation retrieval has been 1) using the single-scattering properties (SSPs) derived from ensembles of plausible hydrometeors in radiative transfer models (RTMs) for forward calculations to simulate instrument responses, and 2) matching observed instrument responses with simulated ones to arrive at the retrieved particle ensemble properties (Ding et al., 2016; Kuo et al., 2016; Haddad et al., 2017). Consistent physical estimates so retrieved from these microwave observations thus require SSPs of realistic precipitation particles covering the natural ranges of morphologies and compositions (Haddad et al., 1997; Olson et al., 2016; Munchak, 2018; Kneifel et al., 2018). Therefore, the uncertainty resulting from the assumptions of particle geometries or from their SSP calculations constitutes an upstream source of retrieval uncertainties, which is likely to propagate through the retrieval process and cause irreconcilable errors downstream.

Given the crucial importance of accurate SSPs from realistic hydrometeors to the success of precipitation retrieval algorithms, significant efforts have been devoted, and progresses have been made, in the last couple decades to 1) the enhancement of the realism and complexity of particle models in both geometry and composition through simulated deposition growth, aggregation, riming and/or melting (Liu, 2008; Kuo et al., 2016; Lu et

al., 2016; Eriksson et al., 2018), and 2) the development of computationally efficient numerical methods to solve the electromagnetic (EM) scattering of hydrometeors with irregular shapes and heterogeneous compositions (Bohren & Singham, 1991; Mishchenko, 2014; Fenni et al., 2018). Due to their irregular, complex shapes and uneven distribution of compositions, these hydrometeors do not exhibit symmetries as spheres, spheroids, or other regular convex shapes do. Consequently, their SSPs are orientation-dependent and lack symmetry to exploit. Most of the existing microwave RTMs (Evans & Stephens, 1995; Deeter & Evans, 1998) used to simulate instrument responses, however, are simplified to deal only with axially or azimuthally symmetric scattering medium. The hydrometeors are thus usually assumed to be uniformly randomly oriented. SSPs must therefore be obtained for each hydrometeor at a number of orientations, which are then averaged to produce axially symmetric SSPs.

For solving the EM scattering of these complex hydrometeors, methods based on the discrete dipole approximation (DDA, aka coupled dipole approximation) (Draine & Flatau, 1994; Yurkin & Hoekstra, 2007; Penttilä et al., 2007; Petty & Huang, 2010) have been more generally applicable than other methods, e.g. Mie and T-matrix, for their versatility with respect to the shapes of the scattering target. Thus, several DDA-based codes, e.g. DDSCAT (Draine & Flatau, 2013), ADDA (Yurkin & Hoekstra, 2011), have been used extensively to characterize scattering by arbitrarily shaped precipitation particles (Nowell et al., 2013; Ori et al., 2014; Johnson et al., 2015; Kuo et al., 2016; Eriksson et al., 2018).

There are basically two solution strategies, hence two categories, of DDA implementations, one based on iterative solvers (e.g. DDSCAT and ADDA) and the other on direct solvers (Petty & Huang, 2010). The direct-solver-based (DSB) DDA methods are more efficient when SSPs for multiple orientations are needed because, once the matrix has been inverted, it may be applied to incident waves from different directions (equivalent to varying the orientation of the target while keeping the incident direction constant). However, as the mass of the hydrometeor increases, the number of dipoles and hence the rank of the matrix increases proportionally. Since the computation complexity of matrix inversion is approximately $O(n^3)$ where n is the number of dipoles, the computational cost increases drastically. Moreover, when its rank is high, the matrix is usually less numerically stable to invert.

The iterative-solver-based (ISB) DDA methods, on the other hand, implemented with a Fast Fourier Transform (FFT) acceleration for matrix and vector multiplications in both DDSCAT and ADDA, have a computational complexity roughly proportional to $O(N \log N)$, where N is the number of grid cells, i.e. $N = l \times w \times h$ with l , w , and h for, respectively, number of cells in length, width, and height of the rectangular grid system used to contain the dipoles of the hydrometeor, which is composed of n dipoles. In general, $N > n$ but, for sparse hydrometeors like those studied here, $N \gg n$. Then, each target orientation (incident wave direction) must be solved independently and separately. When different orientations are needed for the scattering target that lack symmetry, as is the case with most solid- and mixed-phase hydrometeors, the computation expense required to obtain solutions increases proportionally with the number of orientations. This is exactly the situation encountered in conducting forward radiative transfer simulations with the great majority of existing RTMs in support of retrieval algorithms for complex hydrometeors.

The contrast of computation complexity, and thus expense, between DSB- and ISB-DDA methods can be illustrated with a simple example. If a hydrometeor requires only $n = 200$ dipoles to represent in a $N = 100^3 (= 100 \times 100 \times 100)$ bounding cubic grid system, i.e. a mere 2×10^{-4} fraction in volume, the DSB- and ISB-DDA methods would already have comparable computation complexity. Even the sparsest snowflakes, e.g. dendrites, are rarely that sparse. Therefore, except for very small and compact particles (few hundred dipoles), the ISB-DDA methods almost always have an advantage in computation efficiency over the DSB-DDA methods, even when the number of orientations has been taken into account. This is the primary reason that the ISB-DDA methods are more popular than the DSB-DDA methods.

A notable anomaly is the recently developed scattering model MIDAS, for MoM Integral-equation Decomposition for Arbitrarily-shaped Scatterers (formerly NESCoP in Fenni et al. 2018), applying a domain-decomposition technique known as the characteristic basis function method (CBFM) to the Method of Moments (MoM) in solving EM scattering. MIDAS belongs essentially to the DSB category, though not a DDA approach. After the application of a Method of Moment (MoM) with piece-wise constant basis functions, in the context of volume integration equation method (VIEM), the CBFM allows for the decomposition of the original matrix of size $3n \times 3n$ into multiple smaller matrices of sizes $3n_i \times 3n_i$ with $n = \sum_i n_i$. Thus, the computation complexity is approximately reduced from $O(n^3)$ to $\sum_i O(n_i^3)$ (Fenni et al., 2016). As a DSB method, MIDAS also effectively solves all orientation at the same time. With the computation efficiency gain from its matrix decomposition, we believe MIDAS offers an optimal balance of the strengths of both the DSB- and ISB-DDA methods, making it a compelling method for solving the EM scattering of complex hydrometeors.

The number of orientations needed for the averaged SSPs to converge depends on the size of the hydrometeor (relative to the wavelength), on the anisotropy of its shape, and on the performance of the quadrature scheme used. Unfortunately, this dependence is not a simple linear relation and is difficult to determine a priori. One may need to experiment with the number of orientations to ensure convergence by gradually increasing it. We are therefore motivated to use the highly computationally efficient MIDAS to evaluate the efficacy of several quadrature schemes (Hardin & Sloane, 1996; Beentjes, 2015), namely adaptive quadrature (aq), Lebedev quadrature (lb), and spherical design (sd), in minimizing the number of orientations, and hence computation resource, needed for an acceptably accurate orientation average.

Several past studies have discussed the convergence of the orientation-averaged SSPs of atmospheric particles and devoted attention to optimal averaging schemes (Okada, 2008; Penttilä & Lumme, 2011; Um & McFarquhar, 2013). Mainly because of the computational burden associated with the use of the DDA-based codes, none of these studies has involved an as wide and varied set of complex-shaped particles, nor as large numbers of target orientations as this study, which checks more extensively the convergence of averaged SSP and provides a more comprehensive comparison of the numerical average methods selected for evaluation.

Thus, we benchmark MIDAS against a popular ISB-DDA method, i.e. DDSCAT, in our evaluation of the quadrature schemes. We detail the background of our study in section 2 with introductions to and descriptions of relevant previous works, the hydrometeors used in this study, and the scattering codes used, i.e. DDSCAT and MIDAS. After introducing the notations and definitions used in this paper, we compare the differences between the existing and the new approaches with respect to orientation averages in section 3. We report next, in section 4, the impacts of quadrature schemes on the convergence of orientation-average and on computational cost, contrasting MIDAS with DDSCAT. Section 5 concludes and outlines our plans for MIDAS.

2 Context of the study

2.1 Snow particles

We use a subset of the realistic solid-phase aggregate snow particles described in (Kuo et al., 2016) for this evaluative study. The aggregate snow particles are made of pristine ice crystals, which are numerically grown using the algorithm pioneered by Gravner and Griffeath (2009) nicknamed “Snowflake”. The pristine crystals of various sizes are then numerically aggregated to form the aggregate snow particles that span the range of particle shapes and sizes that may occur naturally. The resulting geometries and their SSPs, derived with DDSCAT, of 6646 aggregate particles have been cataloged in the database OpenSSP

and made available at `ftp://gpmweb2.pps.eosdis.nasa.gov/pub/OpenSSP/`. In Figure 1, we show three examples of aggregate snow particles from the OpenSSP database.

The noteworthy feature of the particles from the OpenSSP database is their irregular and complex geometry, which presents a significant challenge and an arduous test for the flexibility and computational efficiency of the scattering solution approaches and the numerical averaging schemes considered in this paper.

2.2 The DDA-based code DDSCAT

The discrete dipole approximation (DDA), also known as the coupled dipole approximation, is a general, versatile method for computing EM scattering by particles of arbitrary geometry and dielectric composition (Purcell & Pennypacker, 1973). The principle of the DDA is to replace the scatterer by a set of point dipoles, often organized in a rectangular lattice of cubic cells, with a grid spacing that is small enough to adequately represent the geometry of the particle and ensure a sufficiently accurate solution. Each dipole ($j = 1, \dots, N$), located at position \mathbf{r}_j , has a polarization $\mathbf{P}_j = \alpha_j \mathbf{E}_j$, where α_j is the dipole polarizability and \mathbf{E}_j is the electric field at \mathbf{r}_j due to the incident wave \mathbf{E}_j^{inc} plus the contribution of each of the other $N - 1$ dipoles ($k \neq j$). As detailed in Draine & Flatau (1994), solving the scattering problem amounts to solving the system of $3N$ complex linear equations $\sum_{k=1}^N \mathbf{A}_{jk} \mathbf{P}_k = \mathbf{E}_j^{inc}$, where \mathbf{A}^{jk} is a 3×3 matrix, equal to α_j^{-1} if $j = k$, and including retardation effects if $j \neq k$, so that $-\mathbf{A}_{jk} \mathbf{P}_k$ represents the electric field at \mathbf{r}_j due to dipole \mathbf{P}_k at location \mathbf{r}_k . Once this system is solved for all unknown polarizations \mathbf{P}_j , $j = 1, \dots, N$, all the scattering quantities of interest (extinction, absorption, scattering, backscattering, asymmetry parameter) can be directly evaluated from the resultant polarizations (Draine, 1988; Draine & Flatau, 1994; Yurkin & Hoekstra, 2007).

Because of its flexibility and applicability to arbitrary geometries, DDA-based methods have been extensively used to calculate the SSPs of hydrometeors. The two most popular implementations of the DDA are the open-source codes DDSCAT (Draine & Flatau, 2013) and ADDA (formerly, Amsterdam DDA, Yurkin & Hoekstra, 2011). Penttilä et al. (2007) documented the accuracy and computational performance of four different implementations of DDA by comparing them to exact techniques. They conclude that 1) DDSCAT is the most accurate and 2) ADDA is the fastest and least memory consuming code, by virtue of its efficient MPI implementation, which parallelizes a single DDA computation by grouping together memories of multiple processors, and thus allowing the solutions of large particles.

In this study, we use DDSCAT to test and validate the accuracy and computational performance of our MoM/CBFM-based model MIDAS by applying both to the calculation of orientation-averaged scattering efficiencies. The choice of using DDSCAT as a benchmark is justified by its high accuracy and being the second fastest code among those evaluated in Penttilä et al (2007). In addition, the MIDAS version evaluated here uses OpenMP for shared-memory parallelization similar to DDSCAT¹. In such a configuration, the efficient MPI parallelization does not confer ADDA a significant advantage in speed over DDSCAT.

The value of present study is signified by the shortcomings of the DDA-based codes when calculating orientation-averaged SSPs. These quantities are crucial to the well-functioning of the precipitation retrieval algorithms. In fact, a major drawback of the DDA is its high computational cost when the calculations are performed over a large number of particle orientations. Because of the use of iterative solvers, the computationally demanding linear equations must be solved repeatedly for each orientation. Yet it is well known that preference has been given to iterative methods, mainly because of the prohibitive memory cost of storing

¹ The claimed MPI capability of DDSCAT simply runs an independent calculation, e.g. a different orientation, on each computer node of a cluster in a pleasingly parallel manner and does not group nodes' memories together for distributed parallelism as ADDA is capable of.

the entire matrix for the direct solvers (Yurkin & Hoekstra, 2007). In the next section, we will explain how the CBFM, a powerful direct-solver-based (DSB) domain-decomposition scheme, enables computationally efficient direct solution for multiple-excitation problems, and thus simulation of particles with large number of orientations, with lower computational resource requirements than DDSCAT.

2.3 The MoM/CBFM-based scattering model MIDAS

Fenni et al (2018) documents our development of MIDAS (formerly NESCoP), a numerically efficient 3D full-wave model for scattering from complex-shaped scatterers. The main concept in MIDAS is the use of a DSB domain-decomposition method in the context of the volume integral equation method (VIEM) to efficiently compute scattering properties of electrically and numerically large precipitation particles. First, the VIEM is linearized with the conventional Method of Moments (MoM), with piecewise constant basis functions. We refer readers to Fenni et al. (2018) for further details about the volume integration formulation and the application of the MoM. As a result we obtain a system of linear equations $\mathbf{Z}^{MoM} \mathbf{E} = \mathbf{E}^{inc}$, where \mathbf{Z}^{MoM} is the MoM matrix of size $3n \times 3n$, \mathbf{E}^{inc} is the incident field and \mathbf{E} is the unknown total electrical field inside the particle. The MoM solution is essentially of the same form as in the DDA. "The only difference between the two approaches is that the integral equations give more mathematical insight into the approximation, thus pointing at ways to improve the method, while the model based on point dipoles is physically clearer" (Yurkin & Hoekstra, 2007).

The next step is to apply the domain decomposition method known as the Characteristic Basis Function Method (CBFM) (Mittra & Du, 2008; Lucente et al., 2008). The basic idea of a domain decomposition method is to replace the numerically large global EM problem with smaller, more manageable independent local problems, while using appropriate coupling conditions between the sub-domains. The particular feature that distinguish the CBFM from other domain decomposition methods is its use of a direct solver to calculate the unknown electric field inside the global domain (Lucente et al., 2008). The CBFM operates by generating a new set of S_i basis functions, named characteristic basis functions, for each sub-domain ($i = 1 : M$), whose purpose is to reduce, as much as possible, the overall numerical size (n) of the EM problem. A more efficient direct solver can then be implemented to solve the resulting compressed system of linear equations $\mathbf{Z}^c \boldsymbol{\alpha} = \mathbf{E}^{inc,c}$. \mathbf{Z}^c is the resulting compressed matrix, of size $K \times K$, where $K = \sum_{i=1}^M S_i$, and $\boldsymbol{\alpha}$, of size $K \times \mathcal{N}_D$, contains the coefficients used to calculate the total electric fields inside the object, for \mathcal{N}_D incident directions, as a linear combination of the new sets of basic functions.

The size-reduction of the initial MoM matrix is quantified through the compression rate CR , which is defined as the ratio between the original number of basis functions in the x , y and z directions and the number of post-CBFM unknowns : $CR = 3n/K$. The CBFM is thus much better adapted to the calculation of averaged scattering quantities, because the compressed system of linear equations is solved once for all incident directions, i.e. multiple excitations. Once the electric field inside the snow particle is known for the \mathcal{N}_D incident directions, the scattered field \mathbf{E}^s can be calculated at any scattering direction, and its computation cost at \mathcal{N}_{SCA} observation points scales as $O(n \times \mathcal{N}_D \times \mathcal{N}_{SCA})$. Readers are referred to Fenni et al. (2018) for further details about MIDAS (previously NESCoP) and the CBFM process.

Accuracy and computational efficiency of an OpenMP-parallelized version of MIDAS are validated against DDSCAT in Fenni et al. (2018) by applying it to calculating the SSPs of ice aggregates from the OpenSSP database (Kuo et al., 2016). We have observed good agreements between them, as long as the iterative solver used by DDSCAT does not encounter numerical convergence problems. We have also noticed that the performance of DDSCAT, in both accuracy and computational efficiency, strongly depends on the size of the rectangular container of the particle and its density of non-trivial dipoles, while MIDAS

offers a more constant level of accuracy and faster time to solution. We have expected the superior performance of MIDAS over DDSCAT in situations where a large number of orientations are requested. We, however, have pleasantly found that, even for solving the SSPs at one single orientation, MIDAS outperforms DDSCAT in computing time when the size parameter gets large (Fenni et al., 2018).

3 Calculation of Orientation Averages

3.1 Notations and Definitions

The topic discussed here is evidently complex, for which similar or equivalent but different terms may be used in the literature to refer to or describe various concepts. To avoid confusion, we define the terms and associated concepts that will be consistently used in the following discussions. In this paper, we use two quantities to describe the scatterer's "size" relative to the wavelength at which the scattering solution is sought. One involves the maximum dimension, D_{max} , which is the distance between the farthest two points within the scatterer or, equivalently, the diameter of the smallest sphere that encloses (or circumscribes) the scatter. We call it "electrical size" of the scatterer, and defined it as

$$x_d = \pi D_{max} / \lambda \quad (1)$$

Another is x_e , using the equivalent volume sphere diameter D_e , i.e.

$$x_e = \pi D_e / \lambda \quad (2)$$

Together, x_d and x_e give an indication of the sparsity of the scatterer. With the same x_e , a scatterer with a larger x_d is considered to be sparser than the one with a smaller x_d , i.e. the latter is more compact.

Due to the priority given to expediency, weather models and retrieval algorithms use simplified one-dimensional (1D) RTMs that can only handle media with axially (or azimuthally) symmetric scattering, which SSPs derived from irregularly shaped particles do not possess. These particles are therefore assumed to be uniformly (i.e. non-preferentially) randomly oriented and their SSPs must be orientationally averaged to attain the required symmetry. Two questions thus arise: (1) how to determine the number of particle orientations required for orientation-averaged SSPs to converge and (2) how to achieve convergence with a minimum number of orientations. The goal is to incur the lowest computational cost for any electrical size regardless of the complexity of particle geometry. The popular DDA codes provide no convenient answers to the above two questions because 1) their interfaces offers only the simplest sampling of the orientation angles for average and, more importantly, 2) the computational cost becomes prohibitive with these codes for electrically large particles and a large number of orientations.

DDSCAT and MIDAS use different but equivalent conventions for specifying scatterer orientation. DDSCAT rotates the scatterer in θ and β as defined in its user guide, whereas MIDAS reorients the direction of the incoming EM wave while holding the scatterer fixed in space. The incident direction (ID) of MIDAS, (θ_i, ϕ_i) , is related to the scatterer's orientation in DDSCAT, (θ, β) , through the relations:

$$\theta_i = \theta ; \phi_i = (\beta + \pi) \mod 2\pi \quad (3)$$

with the subscript i here denoting "incident" (i.e. not a dummy running index). With this equivalence established, we shall use primarily (θ_i, ϕ_i) in describing orientation to simplify our discussion.

We also recall that the scattering quantity of focus is the polarization-averaged backscatter efficiency. Thus, we do not consider polarization rotation, and we only change the in-

cident wave direction by varying θ_i and ϕ_i as described in Fig 2. With DDSCAT, this is equivalent to fixing the third angle (ϕ) at 0 and changing only the β and θ angles for specifying the target orientation of the particle. For DDSCAT, the ϕ rotations do not affect the polarization-averaged scattering quantities, nor does it have a significant impact on the computational cost (Draine & Flatau, 2013). Thus, for the present study we will only vary the β and θ angles for DDSCAT. Note that this is equivalent to varying the β and γ angles for ADDA.

Scattering calculations reported in this paper are performed with OpenMP-parallellized versions of MIDAS and DDSCAT run on a single large-memory computing node of 48 CPUs and 380 GB of RAM. Comparisons between MIDAS and DDSCAT are usually expressed using relative difference in percentage, which is defined based on the difference between a quantity, Q , and its corresponding reference, Q_r , i.e.

$$Er(\%) = 100 \times (Q - Q_r)/Q_r \quad (4)$$

when comparing SSPs obtained from the MIDAS and DDSCAT methods, the solution of DDSCAT is used as the reference.

In the following subsections, we first describe the orientation-average approach implemented in DDSCAT, and then the one used with MIDAS previously in Fenni et al (2018). We describe next the process of defining and achieving the convergence of the averaged SSPs. We then evaluate two quadrature schemes over the sphere, namely Lebedev quadrature (lb) and Spherical Design (sd). These schemes are selected based on their reported good performance (Beentjes, 2015).

3.2 DDSCAT

For DDSCAT, orientation-averaged scattering quantities are computed by fixing the incident wave direction and evaluating the scattering over a number of particle orientations. For a uniformly randomly oriented target with no symmetry, the orientational average \overline{Q} of a quantity $Q(\beta, \theta, \phi)$ is calculated as follows

$$\overline{Q} = \frac{1}{8\pi^2} \int_0^{2\pi} d\beta \int_{-1}^1 d\cos\theta \int_0^{2\pi} d\phi \quad Q(\beta, \theta, \phi) \quad (5)$$

where $(\beta, \theta$ and $\phi)$ are the angles describing the 3D orientation of the snow particle (Draine & Flatau, 2013). Given that the focus of this study is on the calculation and convergence of orientation-averaged backscatter efficiency (\overline{Q}_{bks}), a scalar quantity independent of polarization, Eq. 5 is re-written as:

$$\overline{Q} = \frac{1}{4\pi} \int_0^{2\pi} d\beta \int_{-1}^1 d\cos\theta \quad Q(\beta, \theta) \quad (6)$$

Indeed, the backscatter efficiency Q_{bks} is the most sensitive scattering quantity to the particle shape and to the parameters of the scattering model. We refer the reader to Bohren & Singham (1991) for the physical insight into backscattering that explains this sensitivity. Thus, ensuring the convergence of \overline{Q}_{bks} automatically guarantees the convergence of other scattering quantities, namely the orientation-averaged extinction and scattering efficiencies.

After one has solved the scattering problem for a given (β, θ, ϕ) , the solutions corresponding to other values of ϕ , while holding β and θ constant, are efficiently obtained by appropriately weighted sums of the solutions found at (β, θ, ϕ) . Thus, averaging over ϕ is relatively inexpensive and most of the computational cost is associated with the number of different (θ, β) (Draine & Flatau, 2013).

DDSCAT offers a default sampling scheme through its input file (i.e. `ddscat.par`), which samples uniformly in β and $\cos\theta$ in equi-interval manner. The range for β (2π for the entire sphere) is simply divided into \mathcal{N}_β equal intervals, and the midpoint of each interval is taken. Sampling in θ is done quite differently. The parity of \mathcal{N}_θ determines the equi-interval samples over $\cos\theta$: A simple arithmetic sum is used if \mathcal{N}_θ is even while Simpson's rule is used if it is odd. Therefore, if averaging over orientations is desired, Draine & Flatau (2013) recommends an odd value of \mathcal{N}_θ be specified for greater accuracy. In the remainder of the paper, this sampling scheme will be abbreviated to 'dn', short for DDSCAT native quadrature.

3.3 MIDAS

Instead of rotating the target, MIDAS equivalently changes the incident wave to the counter direction of the target rotation. Thus, holding the particle fixed, the averaging is performed over a number of incident wave directions (θ_i, ϕ_i) as follows

$$\overline{Q} = \frac{1}{4\pi} \int_0^{2\pi} \int_0^\pi Q(\theta_i, \phi_i) \sin\theta_i \, d\theta_i d\phi_i \quad (7)$$

where (θ_i, ϕ_i) describes the direction of the incident wave, referred to as ID, as illustrated in Figure 2.

For MIDAS, the integral over the incident directions, in Eq. 7, is evaluated by a double use of a tailored subroutine QAG from QUADPACK (Piessens et al., 1983), a FORTRAN90 library routine for numerical integration using adaptive quadrature. With the approximated function f as input, the original QAG is a simple globally adaptive integrator that calculates an approximation to a definite integral $I = \int_a^b f$, using a Gauss-Kronrod quadrature rule, while adapting the quadrature nodes, and thus refining the sub-intervals of the integration domain.

In our case, we provide, as input to the QUADPACK subroutine QAG, the values of the scattering quantity under consideration (here Q_{bks}) at \mathcal{N}_D nodes uniformly spaced in θ_i and ϕ_i on the sphere surface. $\mathcal{N}_D = \mathcal{N}_{\theta_i} \times \mathcal{N}_{\phi_i}$, where \mathcal{N}_{θ_i} is the number of nodes for θ_i and \mathcal{N}_{ϕ_i} the number of nodes for ϕ_i . The program exits when convergence is achieved or the sub-interval refinement goes beyond the provided grid resolution ($d\theta_i$ or $d\phi_i$). Since we pre-compute Q_{bks} at the \mathcal{N}_D nodes, we do not in actuality benefit, in reduced computation time, from the adaptive reduction in number of nodes offered by QAG. But we do make the most use out of QAG for its adaptive approximation improvement and accuracy refinement features and its core Gauss-Kronrod quadrature rule. As an illustration, if we calculate the SSPs with a uniform step in θ_i and ϕ_i , $d\theta_i = d\phi_i = 10^\circ$, we would provide 37 evaluation nodes to the outer integral (in ϕ_i) and 19 ones to each of the 37 inner integrals (in θ_i), which represent in total the 703 nodes of the grid.

As described previously, both MIDAS incident directions and DDSCAT target orientations will be referred to as IDs in the rest of the paper. For example, calculating Q_{bks} using DDSCAT with dn and 703 IDs means running DDSCAT with its native quadrature scheme, with $\mathcal{N}_\phi = 1$ and $\mathcal{N}_\theta \times \mathcal{N}_\beta = 703$ total target orientations. Figure 3 shows the distribution of 703 quadrature nodes for MIDAS aq (left) and DDSCAT dn (right).

3.4 Discrepancy in Orientation Averages

When comparing scattering efficiencies at individual incident directions, i.e. at exactly the same ID, the results from MIDAS and DDSCAT have always shown fairly good agreement. However, we have noticed large differences between MIDAS and DDSCAT when it comes to orientation-averaged scattering quantities, particularly for aggregates with large size parameters, pointing to performance disparity in the different quadrature

schemes used by the methods. Figure 4 shows the relative difference observed between MIDAS and DDSCAT solutions in the extinction and backscatter efficiencies, Q_{ext} and Q_{bks} , and asymmetry parameter, g , at 12 frequencies equally spaced from 15 to 200 GHz, for a complex-shaped snow particle with an equivalent volume sphere diameter of $D_e = 3.22$ mm, a maximum dimension of $D_{max} = 11.45$ mm, and a particle size parameter of $x_e = 6.74$ at the highest considered frequency $f = 200$ GHz.

Recalling the definition of the relative difference Er , i.e. Equation 4, Figure 4a shows that the results are in good agreement at a given orientation, but a difference up to 18% arises for Q_{bks} when averaged over 180 IDs for DDSCAT ($\mathcal{N}_{\theta_i} = 18$ and $\mathcal{N}_{\phi_i} = 10$) and 231 IDs for MIDAS ($\mathcal{N}_{\theta_i} = 11$ and $\mathcal{N}_{\phi_i} = 21$) (Figure 4b). Similar differences (not shown here) are observed for Q_{bks} in results obtained from MIDAS with $\mathcal{N}_{ID} = 703$ and 2701 incident directions, using uniform step of 10° and 5° , respectively in both θ_i and ϕ_i .

It is worth noting that a good agreement is maintained between MIDAS and DDSCAT for the averaged extinction coefficient \overline{Q}_{ext} and asymmetry parameter \overline{g} , which confirms the higher sensitivity of Q_{bks} to orientation. The exorbitant computational cost associated with DDSCAT for a large number of target orientations prohibits us from calculating the SSPs using a larger \mathcal{N}_{ID} at all 12 frequencies, on the 64 GB/16 CPU/8 day wall-time server that was used by the time of the previous study (Fenni et al., 2018)). Indeed, as can be seen in Figure 4b, re-drawing Figure 17b of Fenni et al. (2018), no result is plotted at $f = 200$ GHz because this particular DDSCAT run exceeded the 8-day (i.e. 192-hour) wall-time quota allocated to us on that previous server without completing.

Given the importance of Q_{bks} in radar retrieval algorithms, it is crucial to understand the source of the observed difference in averaged backscatter efficiency, \overline{Q}_{bks} , and to verify that this difference is not due to an error in our MIDAS EM solution. To do so, we have run DDSCAT at exactly the same orientations as those used in MIDAS with the aq configuration. Using the same aq quadrature scheme helps isolate the contribution by the EM scattering solution method to the observed difference.

Figure 5 shows a comparison of Q_{bks} obtained from MIDAS and DDSCAT as functions of θ_i and ϕ_i at $f = 50$ and 133.3 GHz, where the orientation-averaged Q_{bks} values from MIDAS and DDSCAT show the greatest discrepancies (Figure 4b). With a relative difference no greater than 7% in absolute value, we can tell that the observed discrepancy is not likely caused by the EM scattering solution, but by the difference in the quadrature scheme. This is verified in Figure 6 which shows Q_{bks} at 50 GHz for the MIDAS aq with 231 IDs and DDSCAT dn with 180 IDs, resulting in the large difference in \overline{Q}_{bks} seen in Figure 4b. A new DDSCAT simulation using dn with 231 IDs by specifying $\mathcal{N}_{\theta_i} = 11$ and $\mathcal{N}_{\phi_i} = 21$ is also shown (3rd row of Figure 6). Thus, both MIDAS and DDSCAT use the same number of quadrature nodes, i.e. $\mathcal{N}_{ID} = 231$, in Figure 5 and in the 1st and 3rd rows of Figure 6, whereas a smaller number, i.e. $\mathcal{N}_{ID} = 180$, is used with DDSCAT in the 2nd row of Figure 6. However, while the same quadrature scheme, i.e. aq, is used in Figure 5, different ones, i.e. aq and dn, are used for MIDAS and DDSCAT, respectively, in Figure 6. One can see that using an equal number and comparable distribution of nodes improves the agreement in \overline{Q}_{bks} between the DDSCAT dn and MIDAS aq quadrature schemes.

To summarize, these observations demonstrate the importance of the numerical integration process, namely the quadrature scheme and the number of quadrature nodes, to ensure the accuracy and convergence of the orientation-averaged SSPs, especially for \overline{Q}_{bks} , which will be the focus of the rest of this paper. Given that computational cost increases with the number of nodes (i.e. orientations), especially for DDA methods, more efficient quadrature schemes that can achieve similar accuracy as aq or dn but with fewer nodes are thus desirable. We introduce two such efficient schemes, Lebedev quadrature and Spherical Design, in the next section.

3.5 Lebedev quadrature and Spherical Design

The selection of Lebedev (lb) quadrature and Spherical Design (sd) schemes for evaluation in this paper is primarily motivated by the comparative study of Beentjes (2015), which assesses several quadrature schemes for integration over the surface of a unit sphere in \mathbb{R}^3 . Figures 4, 5, and 6 of Beentjes (2005) show that the lb and sd schemes require fewer quadrature nodes, compared to the Gaussian Product and Monte Carlo schemes, to achieve integration approximation up to machine precision when applied to a set of test functions with different levels of smoothness. Beentjes (2015) concludes that sd and lb quadratures perform the best under general circumstances.

The Lebedev quadrature grid nodes are constructed to be invariant under the octahedral rotation group. The corresponding set of integration weights are determined by enforcing the exact integration of polynomials (i.e. spherical harmonics) up to a given degree, leading to a sequence of increasingly dense grids analogous to the one-dimensional Gauss-Legendre scheme (Burkardt, 2010b).

A spherical design, on the other hand, is a set of \mathcal{N} nodes on the d -dimensional sphere (d-sphere), S^d , such that the average of any polynomial of degree t or less equals the average value of the polynomial on the whole sphere. In our case $d = 2$, i.e. $S^2 \subset R^3$. Such a set is often called a spherical t -design to indicate the value of t , i.e. the degree of the polynomial. It gives thus a constellation of \mathcal{N} nodes on the surface of a unit sphere with equal weights (i.e. $1/\mathcal{N}$) for use in numerical integration (Burkardt, 2010a; Hardin & Sloane, 1996; R. Womersley, 2017; R. S. Womersley, 2018)

Figure 7 shows examples of the distributions of quadrature nodes for a spherical design (sd; specifically, spherical 21-design) and a Lebedev quadrature (lb) of degree 27. See Beentjes (2015) for detailed mathematical definition and analysis of these two quadrature schemes. In our study, we use the pre-computed numerical values of quadrature nodes and weights from Burkardt (2010b) for Lebedev quadrature. For spherical design, we use the datasets in Burkardt (2010a) derived from Hardin & Sloane (1996) up to a polynomial of degree 21, i.e. p (or t) = 21, corresponding to $\mathcal{N} = 240$, beyond which we use point distributions in Womersley (2017) for up to $p = 325$, corresponding to $\mathcal{N} = 52978$.

4 Application to snow aggregates : convergence and calculation cost

Here, we study the impact of the different quadratures described in the previous section, namely dn with DDSCAT and aq, sd, and lb with MIDAS, on both the speed of convergence for orientation-averaged backscatter efficiency \overline{Q}_{bks} and the computational cost of its calculation, for a large variety of particle geometries and electrical sizes at Ku, Ka, and W bands (13.6, 35.6, and 94 GHz, respectively). The complex refractive indices of ice, determined by interpolation from the tables of Warren and Brandt (Warren, 1984) given at a temperature of 266 K, were $1.7861 + i 3.116 \cdot 10^{-4}$, $1.7861 + i 7.987 \cdot 10^{-4}$ and $1.7863 + i 2.100 \cdot 10^{-3}$ for the Ku, Ka, and W bands, respectively.

For the remainder of the paper, we define relative difference in \overline{Q}_{bks} with respect to a reference value, at which we assert that the \overline{Q}_{bks} has achieved convergence, i.e. reached its stable value of $\overline{\overline{Q}}_{bks}$. This reference $\overline{\overline{Q}}_{bks}$ corresponds to the value achieved using the aq scheme with a number of IDs sufficiently large (more than 7000 IDs), ensuring absolute convergence. We consider the absolute convergence value, and thus the reference $\overline{\overline{Q}}_{bks}$ validated when all aq, sd and lb schemes, used with sufficiently large \mathcal{N}_D , converge within machine precision.

Following Equation 4, the relative difference is thus calculated as $Er(\%) = 100 \times (\overline{Q}_{bks}(\mathcal{N}_D) - \overline{\overline{Q}}_{bks}) / \overline{\overline{Q}}_{bks}$, which describes how far a given \overline{Q}_{bks} is from $\overline{\overline{Q}}_{bks}$, with any of the used integration schemes, at \mathcal{N}_D . Obtaining the accurate $\overline{\overline{Q}}_{bks}$ with certainty for complex-shaped particles is made possible by the high computational efficiency of MIDAS. We were

able to calculate \overline{Q}_{bks} for up to 7800 IDs for various complex-shaped particles, in a few hours each, on a single 48-CPU computing node (see section 3.1), while the computational cost of DDA-based codes had limited the number of target orientations to smaller numbers in previous studies. For example, the maximum number of relevant orientations (not involving polarization rotation) used with ADDA in Um and MaFarquhar (2013) was 33 in θ and 32 in γ totaling 1056 orientations, where, as mentioned in 3.1, the β and γ angles in ADDA are equivalent to, respectively, β and θ angles in DDSCAT.

4.1 Cylinder of Varying Length

We calculated \overline{Q}_{bks} using MIDAS and DDSCAT at Ka band ($f = 35.75$ GHz or $\lambda = 8.4$ mm) of a cylinder with a radius of $r_c = 0.1$ mm and length L varying from 4.2 to 84 mm corresponding to $\lambda/2$ to 10λ . Figure 8 shows the variation of \overline{Q}_{bks} as a function of L depending on the code used (MIDAS or DDSCAT), the quadrature scheme, and the number of incident directions at quadrature nodes used to calculate the averaged scattering quantities. In the figure legend, sd1 refers to the nodes distribution in Burkardt (2010) derived from Hardin & Sloane (1996), whereas sd2 refers to the dataset from Womersley (2017) based on the work described in Womersley (2018), as detailed in section 3.5. For the rest of the paper, sd refers to sd2.

First, as expected, Fig 8 shows that increasing the electrical size of the cylinder results in an increase in the number of nodes required to achieve the convergence, regardless of the quadrature scheme used. Second, \overline{Q}_{bks} clearly converge faster with small numbers of quadrature nodes for sd and lb then for aq or dn (the latter used by DDSCAT only). It is evident that all sd1, sd2, and lb schemes outperform the aq and dn schemes, as we increase the length of the cylinder. Knowing that \overline{Q}_{bks} converged at $L = 10\lambda = 84$ mm with 5400 and 5551 IDs for DDSCAT dn and MIDAS aq respectively, we can see that the sd and lb schemes require significantly smaller numbers of quadrature nodes to converge to the same \overline{Q}_{bks} value. For example, as convergence is reached using DDSCAT with 5400 IDs and MIDAS with 5551 IDs, MIDAS using sd2 with just $\mathcal{N}_{ID} = 482$ achieves \overline{Q}_{bks} within 5% at $L = 10\lambda$. In stark contrast, both MIDAS using aq and DDSCAT using dn with $\mathcal{N}_{ID} = 703$ show relative differences of 244% and 239%, respectively. Similar behavior is observed when the cylinder is rotated around the vertical axis Z (not shown), which confirms the efficiency of the sd and lb schemes regardless of the orientation of the particle.

4.2 Complex Ice Hydrometeors

We compare next the efficacy of the quadrature schemes for orientation-averaged backscatter efficiency (\overline{Q}_{bks}) using complex, realistic snow aggregates. Table 1 lists a set of 10 snow aggregates selected from the OpenSSP database for this study. From left to right, columns 1 and 2 list aggregate id number and images of the particles rendered from two perspectives. The next two, i.e. columns 3 and 4, list respectively size parameter, x_e , and electrical size, x_d , as described in section 3.1. The following three columns list the numbers of IDs required for \overline{Q}_{bks} to achieve relative convergence at W band for the aq, sd, and lb quadratures, respectively. The last column lists, as a reference, the theoretical number of nodes, \mathcal{N}_{th} , according to Yaghjian (1996), required to accurately sample the fields scattered by the particle. For spherical scanning, \mathcal{N}_{th} is derived from equal sample spacing in both ϕ and θ , i.e. $\delta\theta = \delta\phi = \lambda_s / (2.2a + \lambda_s/2)$, where $a = D_{max}/2$ is the radius of the minimum sphere enclosing the particle and $\lambda_s = \lambda / \sqrt{\epsilon'_r}$ is the wavelength inside the scatterer with ϵ'_r being the real part of its relative permittivity to the medium in which the scatter is embedded (Yaghjian, 1996). Observing the duality between the radiated field from and the incoming field towards a minimum sphere, it is logical to argue for the same relation in estimating the theoretical number of incident plane waves needed to accurately represent the scattered field for averaging \overline{Q}_{bks} .

Figure 9 shows, for the snow aggregates in Table 1, except a0012, the convergence of \overline{Q}_{bks} at W band as a function of the number of incident directions for aq, sd, and lb quadrature schemes. \overline{Q}_{bks} is assumed to have achieved relative convergence when the relative difference with respect to the reference is definitively below 1%. Dashed black lines in each panel indicates $\pm 1\%$ of the converged \overline{Q}_{bks} . To ensure absolute convergence, i.e. $\overline{\overline{Q}}_{bks}$, we have used 7800 IDs for aq and 5000 IDs for sd and lb to compute \overline{Q}_{bks} for all the particles listed in Table 1. Almost all of the plots in Figure 9, except for a0012, have been truncated at ≈ 2000 IDs for clarity. It can be deduced from Table 1 and Figure 9, by the lack of correlation between x_e or x_d and \mathcal{N}_{aq} , \mathcal{N}_{sd} , or \mathcal{N}_{lb} , that the rate of convergence does not only depend on the size of the particle but also likely on the anisotropy of its geometry. We, however, have yet to identify a general and reliable rule for the impact of target shape on \mathcal{N}_{ID} needed for \overline{Q}_{bks} to converge. But, it is safe to conclude that sd and lb schemes need far fewer numbers of IDs for \overline{Q}_{bks} of the particles in Table 1 to converge within 1.0% of the references.

In Figures 10-13, we examine more closely the interesting convergence pattern of \overline{Q}_{bks} for snow aggregate a0012, which takes the highest \mathcal{N}_{aq} for \overline{Q}_{bks} to converge, among the 10 particles of Table 1. Snow aggregate a0012 is composed of $N = 46953$ cells/dipoles of size $S_c = 50 \mu\text{m}$, with directional maximum dimensions, along the 3 Cartesian axes, of $(D_x, D_y, D_z) = (7.0, 8.6, 10.7)$ mm. Figure 10 shows the convergence trends of the relative difference (%) in \overline{Q}_{bks} , calculated using DDSCAT and MIDAS with the aq, sd and lb schemes. The relative difference is evaluated with respect to $\overline{\overline{Q}}_{bks}$ computed using MIDAS with the aq, sd and lb schemes for $\mathcal{N}_{ID} > 5000$. First, it is clear that \overline{Q}_{bks} converges faster for the lower frequencies for all quadrature schemes, confirming the impact of the electrical size of the snow aggregate on the number of incident directions required to reach $\overline{\overline{Q}}_{bks}$. The absolute value of the relative difference in \overline{Q}_{bks} falls below 1% for MIDAS and stabilizes at 1.3% for DDSCAT, with fewer than 200 IDs, at Ku band for all the quadrature schemes considered. However, \overline{Q}_{bks} with MIDAS using aq and DDSCAT using dn converge at a much slower rate at W band.

Figure 10 shows that the native scheme used by DDSCAT has the most difficulty to achieve convergence. This observation is confirmed in Table 2, which summarizes the variation of the relative difference in \overline{Q}_{bks} with \mathcal{N}_{ID} for solution methods and quadrature schemes used, as well as the corresponding computational cost. DDSCAT with dn requires more than 7000 IDs to push the relative difference below 5% while only 1891 IDs are needed by MIDAS with aq for a similar performance. In a stark contrast, MIDAS with either sd or lb reduces the relative difference to below 1% for fewer than 500 IDs.

Figures 11-13 provide further insight on the convergence behavior, by showing Q_{bks} value for aggregate a0012 at W band ($f = 94$ GHz) as a function of (θ_i, ϕ_i) with a rainbow color bar in logarithmic scale, visualized on a 2D heat map and a 3D sphere, for four (4) cases, i.e. DDSCAT with dn (Figure 11), MIDAS with aq (Figure 12), lb (Figure 13), and sd (Figure 14). For comparison, results are shown for three (3) progressively greater numbers of IDs (\mathcal{N}_{ID}) in each case. First, one can see that the shape of a0012 exhibits a high degree of anisotropy that causes a particular concentration of large Q_{bks} at the sphere's poles, where the incident direction is perpendicular to the largest pristine surface. The very slow rate of convergence observed for DDSCAT, in comparison to MIDAS, can be then explained by the fact that DDSCAT dn under-samples Q_{bks} near the poles of the sphere (Note the white bands near the poles on the 2D heat maps in Figure 11) where the essential of Q_{bks} variations occur for this particular geometry. This is due to the sampling in $\cos \theta_i$ for DDSCAT dn as opposed to θ_i for MIDAS aq. This therefore means that the convergence speed of \overline{Q}_{bks} , for MIDAS with aq and DDSCAT with dn, is not only impacted by the complex geometry of the realistic snow aggregate, but also by orientation sampling, if there is significant anisotropy. On the other hand, lb and sd schemes perform well with much fewer quadrature nodes irrespective of the complex geometry or orientation of the snow aggregate (see Figures 13 and 14).

Another practical point that differentiates the lb and sd schemes from the classical aq or dn schemes, is that one needs to determine, for lb and sd, only one parameter, namely the number of nodes, while for aq and dn there are two parameters to be determined, namely \mathcal{N}_{θ_i} and \mathcal{N}_{ϕ_i} , which complicates the convergence study. For example, in Um & McFarquhar (2013), 25 different combinations were used for angles β and γ with $\mathcal{N}_{\beta} = 2^j + 1$ and $\mathcal{N}_{\gamma} = 2^k$, where both j and k vary independently from 1 to 5, in order to study the effects of (j, k) on the convergence of averaged single-scattering properties. The conclusion of the authors is that (j, k) does not have a clear impact on the convergence. However, the study of Um & McFarquhar (2013) considers only four (4) geometries and only one (1) of which is of a non-convex shape that can be considered as "complex". Moreover, even this only non-convex geometry is not appreciably anisotropic.

As for computational expense, because DDSCAT is an ISB-DDA code, requiring a large \mathcal{N}_{ID} to achieve convergence in orientation averages, it incurs a large and sometimes prohibitive cost, especially with the default dn scheme for targets of large electrical size. Indeed, combining 1) the iterative solver's limitations with multiple excitations and 2) the low-order of the simple dn scheme used by DDSCAT to compute \overline{Q}_{bks} , particularly for complex, highly anisotropic geometries, makes it very computationally expensive to reach convergence. MIDAS, being a DSB solution, deals much better with problems involving multiple excitations, and rewards us with a significant reduction in CPU time, even for with the similarly low-order aq.

Furthermore, we recall that, for DDSCAT, the primary determinant for computation cost is not the number of dipoles, n , but the number of cells N in the grid system that encloses the target. DDSCAT and ISB-DDA methods in general are thus computationally inefficient for highly porous or sparse particles, for which a large number ($N - n$) of trivial dipoles, must be included to build up a full volume enclosing the particle (Yurkin & Hoekstra, 2007). Therefore, the particle shapes that are more likely to require large numbers of incident directions for \overline{Q}_{bks} to converge are also more computationally expensive for DDSCAT per orientation. The computational cost of MIDAS, however, depends only on the number of non-trivial cells (n), which explains the substantial reduction in CPU time compared to DDSCAT, as seen in Table 2. The use of a high-order quadrature, i.e. lb or sd, reduces the time to solution further, by reducing the number of incident directions (\mathcal{N}_{ID}) required.

It is worth noting that even when DDSCAT engages more computational resources, it does not necessarily outperform MIDAS in time to solution. The simulations involving 4186 and 7125 IDs in Table 2 were run using the pleasingly parallel MPI version of DDSCAT on 10 computing nodes with 16 MPI jobs each, totaling 160 MPI jobs. The two simulations require 40 and 235 min respectively, against 78 min for MIDAS ran with 7381 ID on one single 48-CPU computing node (not shown in Table 2). Note also that Table 2 shows only the computing time with the OpenMP versions of MIDAS and DDSCAT run on a one single computing node.

Finally, to confirm the general superiority in convergence speed and accuracy of the high-order lb and sd schemes over the simple aq scheme, we selected 566 larger snow aggregates from the OpenSSP database to calculate their \overline{Q}_{bks} , using MIDAS with 2701 and 496 IDs for aq, 434 IDs for lb and 482 IDs for sd. We compare 1) the relative difference in \overline{Q}_{bks} , with respect to that obtained with the reference simulation (i.e., aq with $\mathcal{N}_{ID} = 2701$) and 2) the speeds to convergence, when using substantially smaller numbers for \mathcal{N}_{ID} with the aq, sd and lb. We believe that \overline{Q}_{bks} calculated with aq and 2701 IDs legitimately represents the relative convergence as we know that it mostly doesn't vary more than 1% when we increase \mathcal{N}_{ID} to 5329 IDs (not shown here). The D_{max} and D_e of the 566 snow aggregates vary, respectively, from 10 to 15 mm and from 2.2 to 3.5 mm, whereas the number of non-trivial cells n comprising them varies from 43444 and 135780. Figure 15 compares the relative difference in \overline{Q}_{bks} , with respect to aq with 2701 IDs, when using aq with 496 IDs and lb with 434 IDs. Figure 16 shows the same comparison between aq with 496 IDs and sd with 482 IDs. The two figures clearly confirm that the lb and sd schemes require fewer incident

directions than the simple aq scheme to achieve convergence, independent of the shape or size of the snow aggregate. Using comparable low number of incident directions (around 450), the lb and sd schemes estimate \overline{Q}_{bks} with a much smaller relative difference close and concentrated around 0% than the aq scheme. Furthermore, the lb and sd schemes show exactly the same relative difference with respect to aq with 2701 IDs, for the Ku and Ka bands, suggesting that absolute convergence has been secured, at these lower frequencies, for lb with 434 IDs and sd with 482 IDs, as the two quadratures result in the same \overline{Q}_{bks} for all the considered particles.

For the superiority of lb and sd in convergence speed, Figure 17 shows the reduction in CPU time against running MIDAS using aq with 2701 IDs, particularly for the calculation of the scattered field, \mathbf{E}^s , for which the reduction is consistently an order of magnitude. The reduction for the total field, \mathbf{E} , is not as much because the time needed to compute \mathbf{E} inside the scatterer depends more on the numerical size, i.e. n , of the particle and the size of the compressed matrix \mathbf{Z}^c . As the electrical size of the particle increases with the simulation frequency (from left to right), the compression rate achieved by MIDAS decreases resulting in larger \mathbf{Z}^c , and the difference of \mathcal{N}_{UD} starts to impact the time needed to solve the compressed system of linear equations $\mathbf{Z}^c \boldsymbol{\alpha} = \mathbf{E}^{inc,c}$. On the other hand, the time required to compute the scattered field \mathbf{E}^s is directly proportional to the number of incident and scattered directions used to compute \mathbf{E} and the resulting \mathbf{E}^s . Therefore the difference in \mathcal{N}_{UD} has a straightforward impact on the computing time of \mathbf{E}^s independent of the frequency or electrical size of the aggregate. The difference between the first two rows of plots and the third in Figure 17, i.e. as functions of n or x_e versus as function of x_d , confirms that the computational cost of CBFM is mostly determined by the numerical size, i.e. n , of the snow aggregate and, contrary to DDSCAT, is not significantly impacted by its physical extent, i.e. the enclosing rectangular grid system. Thus, we observe a clearer link between the computing time and the parameters (n , x_e) than between the computing time and x_d .

By reducing the number of incident directions required to achieve convergence, independent of the complexity in the shapes of our realistic snow aggregates, the lb and sd schemes significantly enhance the computational efficiency of MIDAS and enable us to generate more accurate orientation-averaged SSPs for realistic hydrometeors with more reasonable computational cost.

5 Conclusions

The constraint of most existing deterministic radiative transfer models (RTMs) to scattering media with axial or azimuthal symmetry necessitates the use of orientationally-averaged single-scattering properties (SSPs) obtained from complex hydrometeors without such symmetries. Thus, the scattering problem must be solved for multiple orientations (or, equivalently, for multiple incident wave directions) for each hydrometeor. The averaging of the orientations, which involves integration over the orientation angles (or incident directions), is then accomplished computationally with numerical quadrature schemes.

The most popular electromagnetic (EM) scattering solution approach for targets of arbitrary shapes has thus far been the iterative-solver-based discrete dipole approximation (ISB-DDA), due to its versatility to complex target geometry and relative computational efficiency over the other approaches. The widely used DDSCAT and ADDA codes are testaments to the success of this approach. However, these ISB-DDA implementations must solve the same scattering problem for each orientation separately. As the required number of orientations increases, their advantage in computational efficiency diminishes. Moreover, the default quadrature schemes offered by these two methods are of rather low order, thus requiring more orientations than higher-order schemes for the orientation average to converge. A user who wishes to use a non-default quadrature scheme must expend considerable effort in configuring the execution of these methods and in organizing the results.

In this paper, we demonstrate that, in contrast with DDSCAT, the advantages of the recently developed MIDAS (Fenni et al., 2018) 1) in solving the EM scattering problem for targets of arbitrary shapes and 2) its inclusion of higher-order quadrature schemes for orientation average. Since MIDAS, based on the Method of Moments (MoM) and using the Characteristic Basis Function Method (CBFM), is a direct-solver-based (DSB) code, it is much more efficient in dealing with multiple incident directions, which constitutes the right-hand side (RHS) of the EM scattering equation $\mathbf{Z}^c \boldsymbol{\alpha} = \mathbf{E}^{inc,c}$ in the form of multicolumned vectors with each vector specifying an incident direction. The compressed system of linear equations is solved once for all considered incident directions. That is, MIDAS does not need to repeatedly solve the same EM scattering problem for each incident direction. Moreover, the use of the CBFM and the associated domain decomposition approach, resulting in compressing the original large MoM matrix, increases significantly the computational efficiency of the MoM-based model. In practice (section 4), MIDAS has demonstrated per-orientation computation superiority over DDSCAT.

Combined with higher-order quadrature schemes, such as Lebedev (lb) quadrature and Spherical Design (sd), the computational advantage of MIDAS is even more apparent, with several orders of magnitude faster time to solution than DDSCAT using its default quadrature. The comprehensive superiority of MIDAS over ISA-DDA methods in accuracy and time to solution makes it a compelling method for solving the EM scattering problem involving complexly shaped and mixed-phase hydrometeors in bands with high refractive-index contrast.

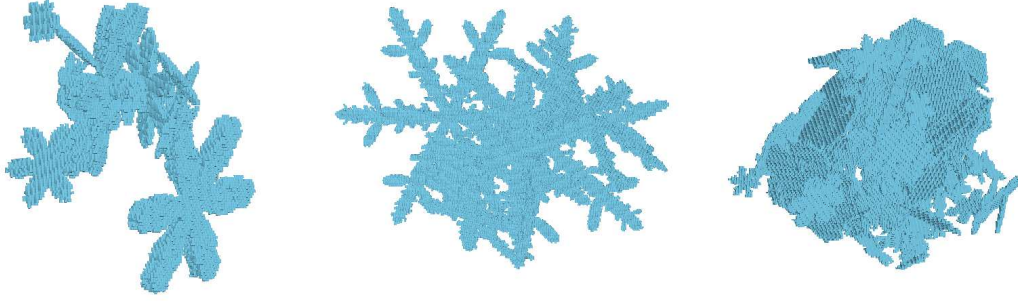


Figure 1: Examples of aggregate snow particles from Kuo et al. (2016). Pristine crystal types are simulated using the Snowflake algorithm (Gravner & Griffeath, 2009), then aggregation simulations are performed to create the aggregate snow particles

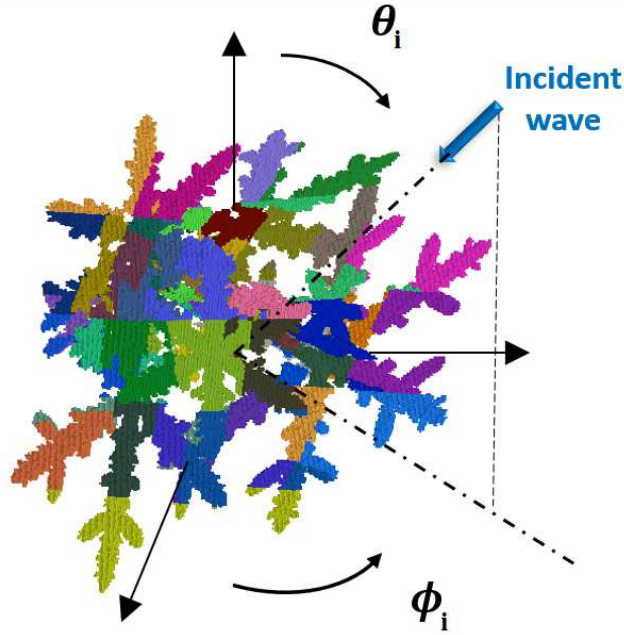


Figure 2: For MIDAS, a snow aggregate is discretized into n cubic cells and divided into M CBFM blocks (different colors). To compute orientation-averaged SSPs, the orientation of the particle is fixed and the direction of the incident wave is described by (θ_i, ϕ_i) .

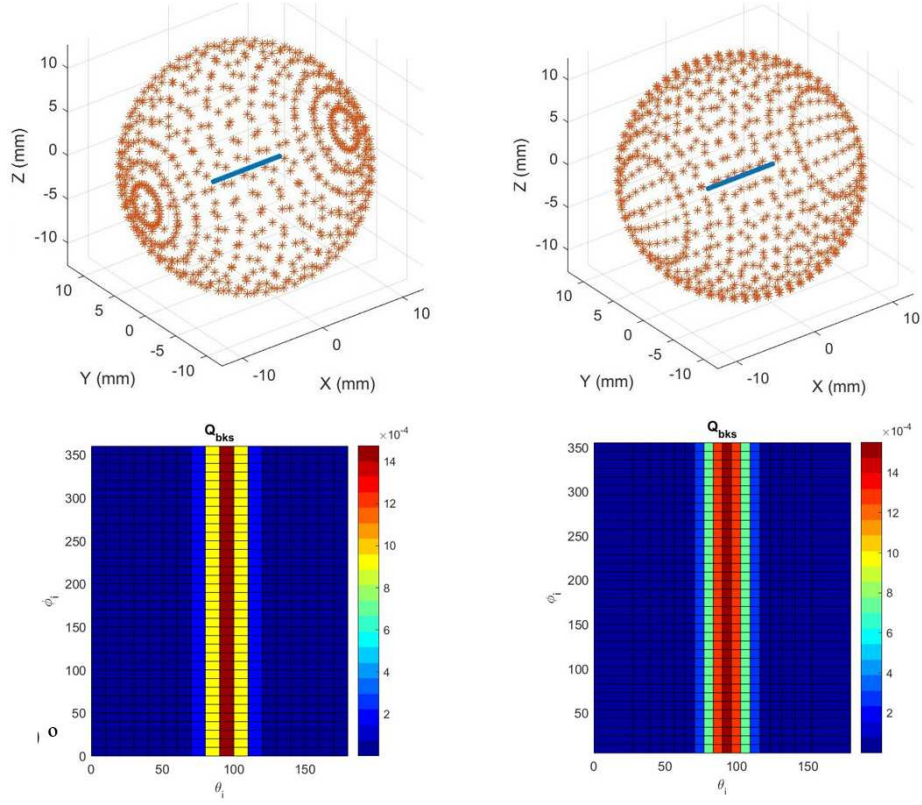
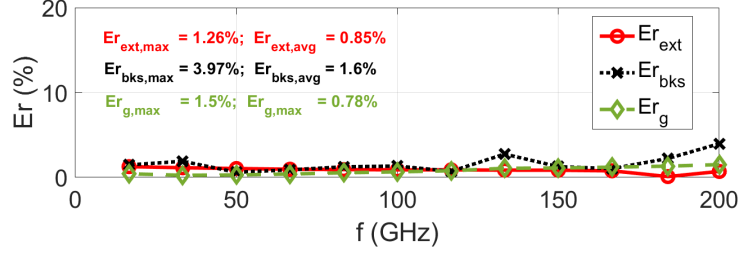
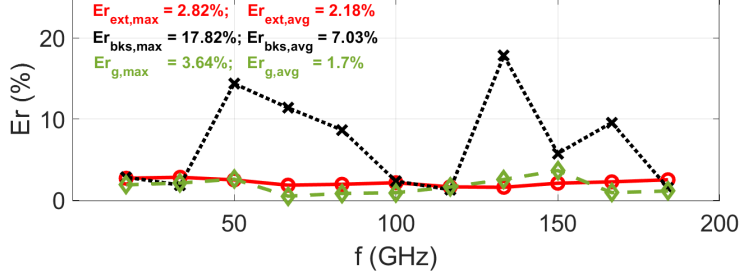


Figure 3: Backscatter efficiency Q_{bks} of a cylinder of length $L = 10\lambda$, as function of incident direction (θ_i, ϕ_i) , calculated for MIDAS (left) with an adaptive quadrature (aq) scheme with $N_{\theta_i} = 19$ and $N_{\phi_i} = 37$ and for DDSCAT (right) with its native quadrature (dn) as function of target orientation-equivalent incident direction with $N_{\theta_i} = 19$ and $N_{\phi_i} = 37$. One can see that, unlike aq, the sampling in $\cos \theta$ by DDSCAT dn does not over-sample the poles.

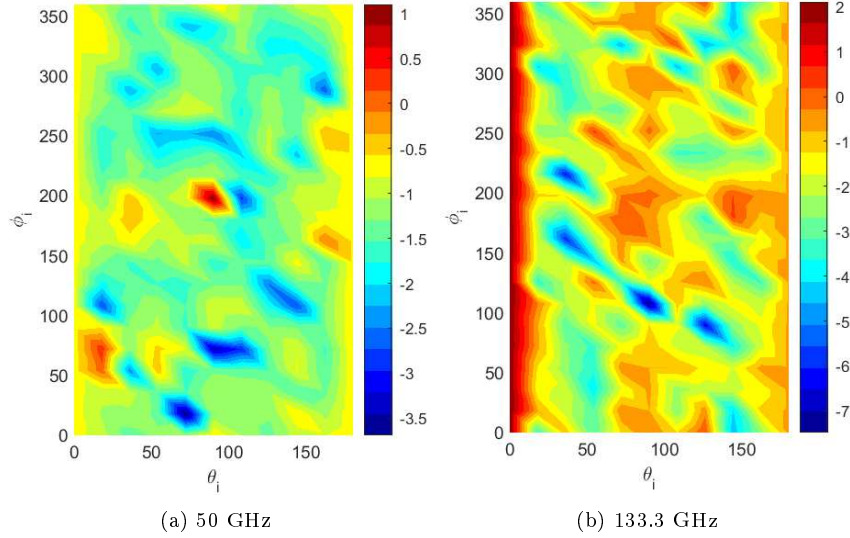


(a) 1 ID



(b) 231 vs 180 IDs

Figure 4: Relative difference, Er , in extinction and backscatter efficiency factors Q_{ext} and Q_{bks} , and asymmetry parameter, g , between MIDAS and DDSCAT, (a) for one ID and (b) when averaged over 231 IDs with MIDAS and 180 IDs with DDSCAT, for a snow aggregate of maximum diameter $D_{max} \approx 10\lambda$ at $f = 200$ GHz.



(a) 50 GHz

(b) 133.3 GHz

Figure 5: The relative difference Er between MIDAS and DDSCAT in backscatter efficiency Q_{bks} , at $f = 50$ and 133.3 GHz, as function of the incident wave direction defined by (θ_i, ϕ_i) . To allow an accurate comparison, we ran DDSCAT at exactly the same orientations as those used in MIDAS with the aq configuration.

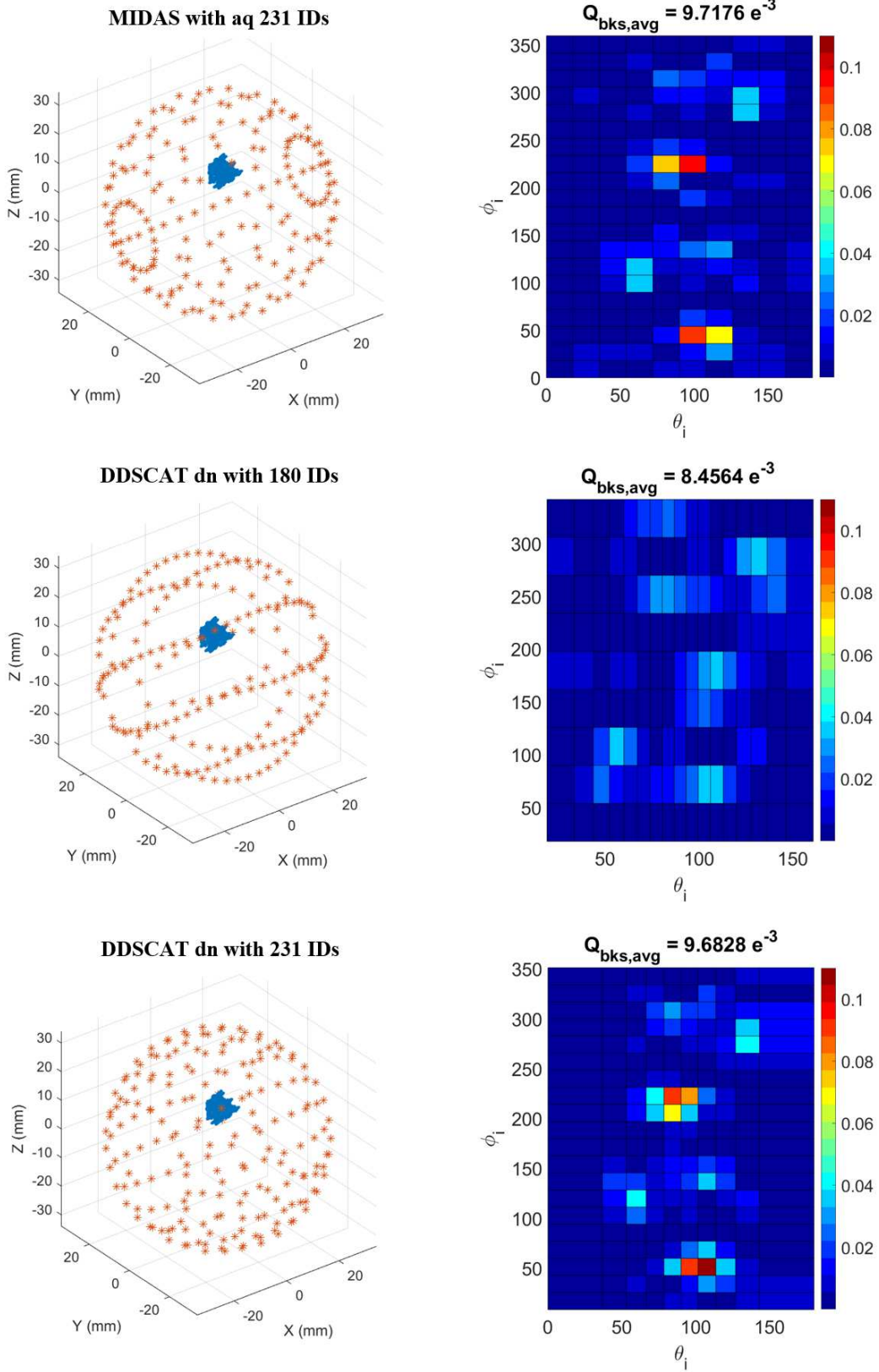


Figure 6: Backscatter efficiency Q_{bks} , at $f = 50$, as function of the incident wave direction calculated with 231 IDs for MIDAS aq (top) and 180 and 231 IDs for DDSCAT dn (center and bottom). The difference between MIDAS and DDSCAT on the Q_{bks} 2D map and thus on the \overline{Q}_{bks} is evident.

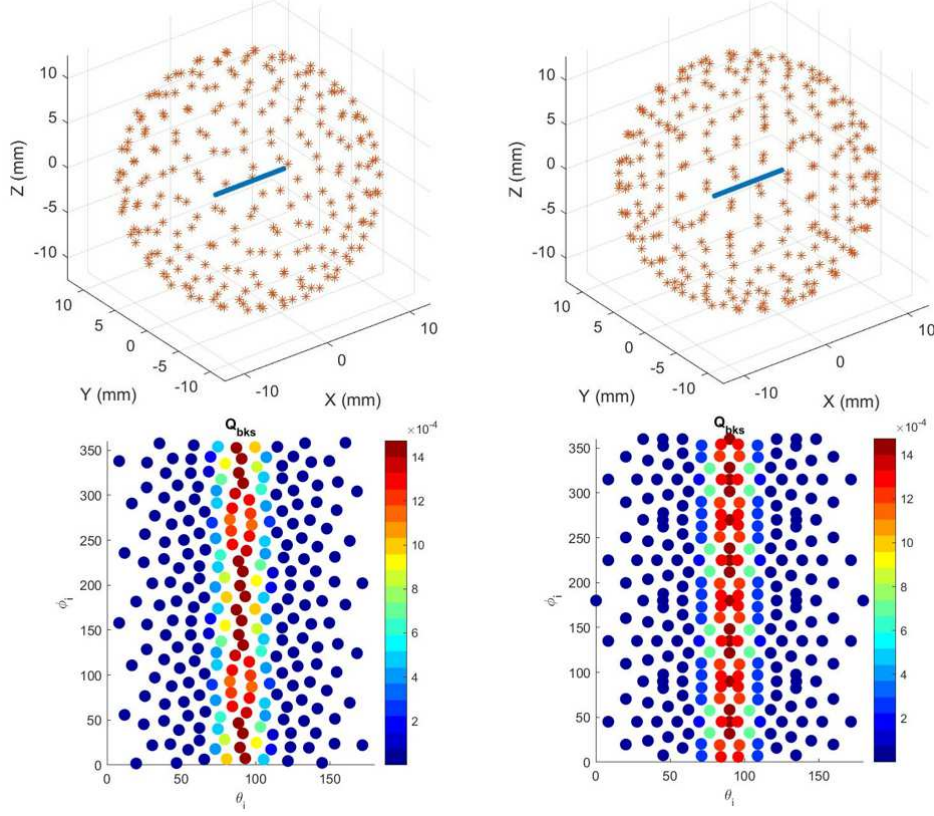


Figure 7: Backscatter efficiency Q_{bks} of a cylinder, as function of incident direction (θ_i, ϕ_i) , calculated with (left) spherical design (sd) at 240 nodes and (right) Lebedev quadrature (lb) at 266 nodes.

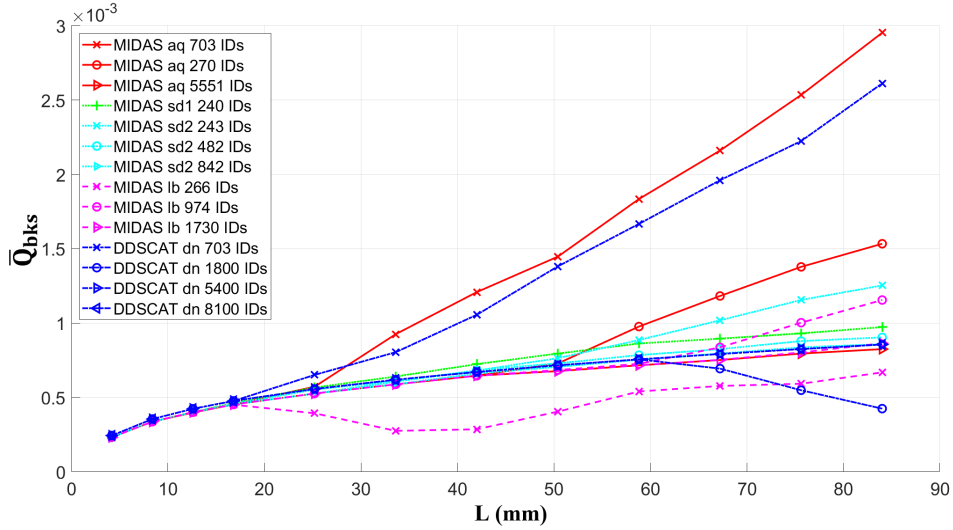
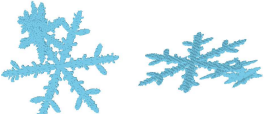
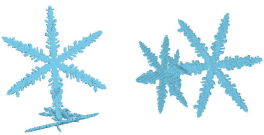


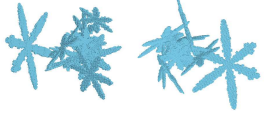
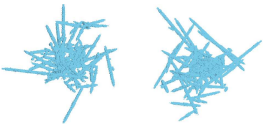
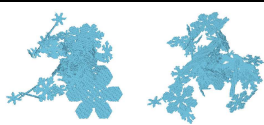
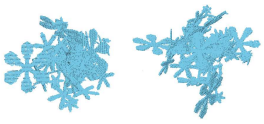
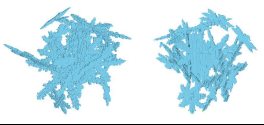
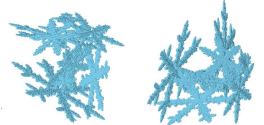


Figure 8: Variations of \bar{Q}_{bks} of a cylinder of radius $r_c = 0.1$ mm, calculated with MIDAS and DDSCAT, as function of the cylinder length L , depending on the used quadrature and the number of nodes. aq, lb and sd, used with MIDAS, refers respectively to adaptive quadrature, Lebedev quadrature and spherical designs.

Table 1: The number of incident directions \mathcal{N}_{aq} , \mathcal{N}_b and \mathcal{N}_{sd} needed for \overline{Q}_{bks} to converge when computed, at W band, with MIDAS and respectively the adaptive quadrature, Lebedev quadrature and spherical designs schemes, depending on the type, geometry and electrical size of the snow aggregate, and the theoretical number of nodes \mathcal{N}_{th} needed to sample the fields radiated by the particle, as function of the electrical size of the aggregate. We assume that Q_{bks} converged if the relative difference with regard to the reference goes below 1% (see example in Figure 10). We recall that x_e and x_d are the size parameters corresponding to D_e and D_{max} , respectively, the equivalent volume diameter and maximum diameter of the particle.

type	geometry	x_e	x_d	\mathcal{N}_{aq}	\mathcal{N}_{sd}	\mathcal{N}_b	\mathcal{N}_{th}
a0027		2.20	10.04	496	482	350	1012
a0012		2.20	10.53	2701	98	434	1104
a0026		2.59	11.02	703	222	434	1200
a0050		2.70	8.07	496	314	230	684
a0017		2.75	11.12	1891	482	350	1200
a0022		2.78	11.62	496	482	434	1300
a0058		2.79	11.76	703	482	434	1326
a0045		2.80	11.57	703	314	350	1300
a0009		3.06	10.53	703	222	350	1104
a0006		3.18	11.27	496	482	230	1225

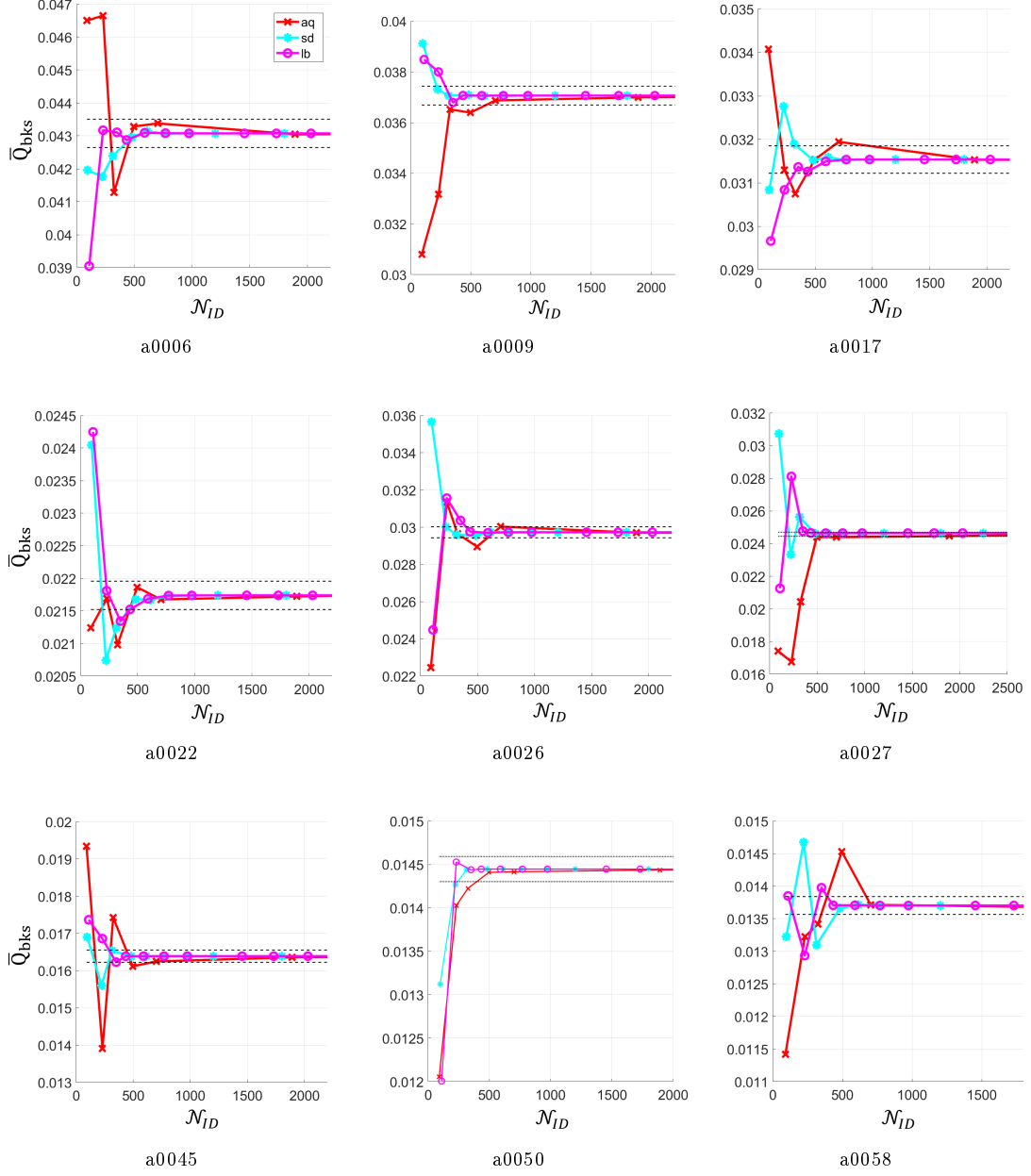


Figure 9: Convergence trends of \bar{Q}_{bks} of nine different snow aggregates computed using MIDAS with the adaptive quadrature (aq), Lebedev quadrature (lb) and spherical design (sd) schemes as function of the number of incident directions (\mathcal{N}_{ID}).

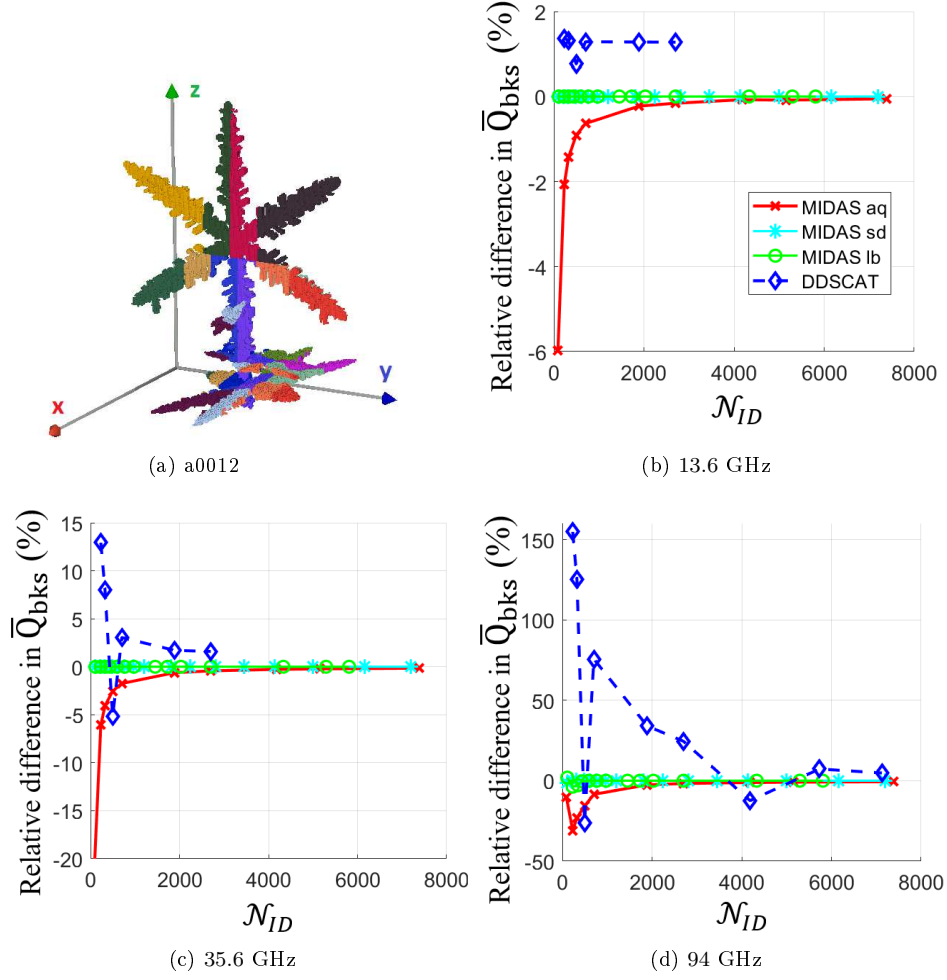


Figure 10: Shape and variations of \overline{Q}_{bks} of the a0012-type particle in Table 1, computed with MIDAS and DDSCAT at Ku, Ka and W bands, depending on the numerical integration scheme used with MIDAS and on the number of incident directions \mathcal{N}_{ID} . The geometry of a0012 is composed of $N = 46953$ cells, divided into 17 CBFM blocks (different colors), for the MIDAS calculations.

Table 2: Relative difference (Er) and computation time in minutes, when using MIDAS and DDSCAT with various quadrature schemes at W band, as function of the number of incident directions (\mathcal{N}_{ID}). The wall time mentioned below is equal to 12 days.

	DDSCAT			MIDAS							
	dn			aq		lb		sd			
\mathcal{N}_{ID}	2701	4186	7125	703	1891	2701	350	590	482	614	
Er (%)	25.0	-12.0	5.2	-8.1	-2.1	-1.3	-2.43	0.4	0.86	0.43	
time (min)	12563	\geq wall time		3	8	15	3.3	3.4	2.6	2.8	

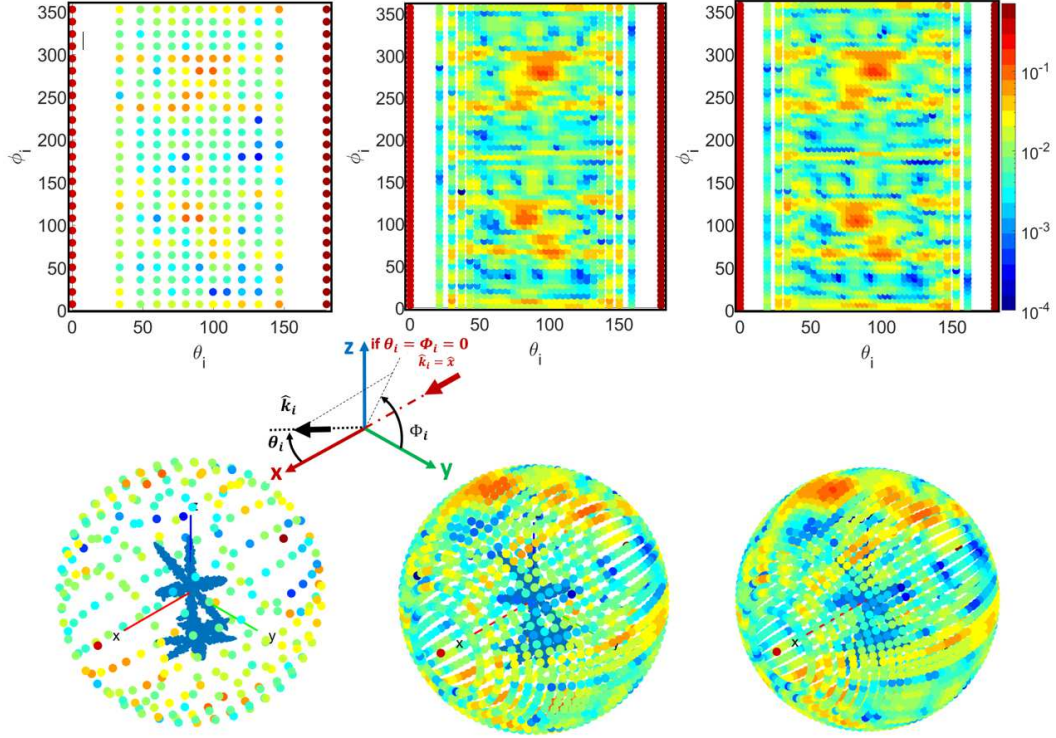


Figure 11: Backscatter efficiency Q_{bks} of a0012, using DDSCAT at $f = 94$ GHz, as function of the incident wave direction (θ_i, ϕ_i) equivalent to the target orientation (θ, β) . (top) 2D scatter plot (bottom) 3D visualization showing the impact of the particle shape on Q_{bks} over the sphere surface, along with the incident direction k_i defined by (θ_i, ϕ_i) . From left to right : Q_{bks} is calculated for 325, 1891 and 2701 IDs resulting in a relative difference E_r (%) in \bar{Q}_{bks} of -125.3% , 34.03% and 25% respectively.

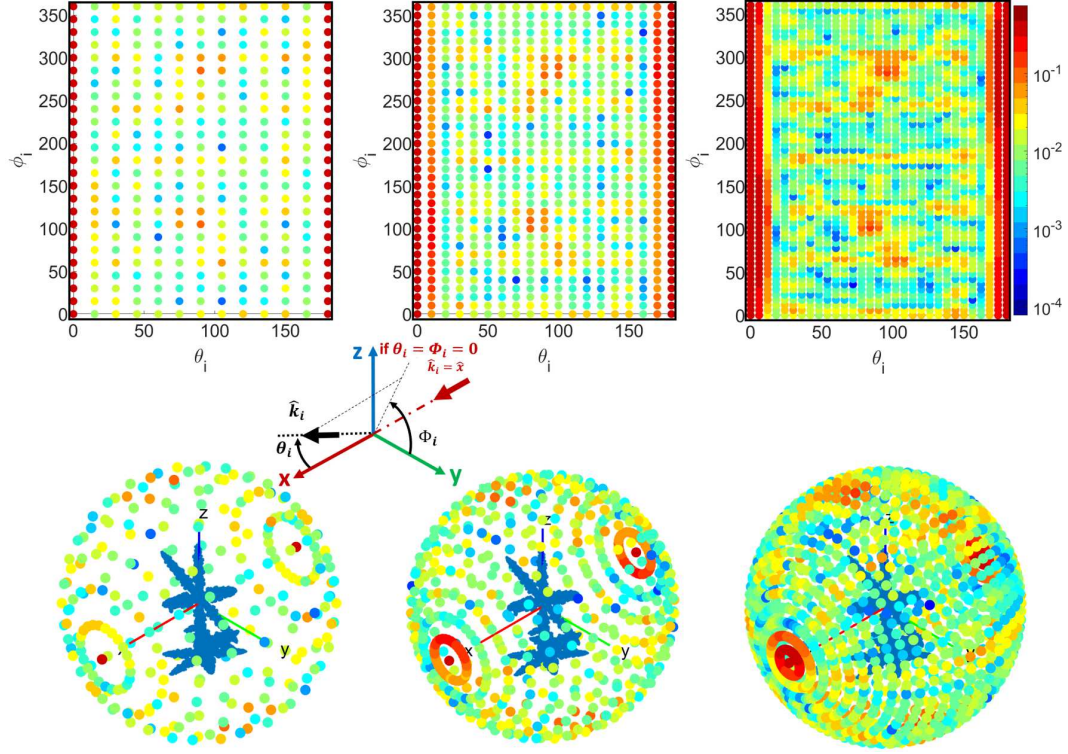


Figure 12: Backscatter efficiency Q_{bks} of a0012, using MIDAS with the aq scheme at $f = 94$ GHz, as function of the incident wave direction (θ_i, ϕ_i) . (top) 2D scatter plot (bottom) 3D visualization showing the impact of the particle shape on Q_{bks} over the sphere surface, along with the incident direction k_i defined by (θ_i, ϕ_i) . From left to right : Q_{bks} is calculated for 325, 703 and 1891 IDs resulting in a relative difference E_r (%) in \overline{Q}_{bks} of -23.1% , -8.1% and -2.1% respectively.

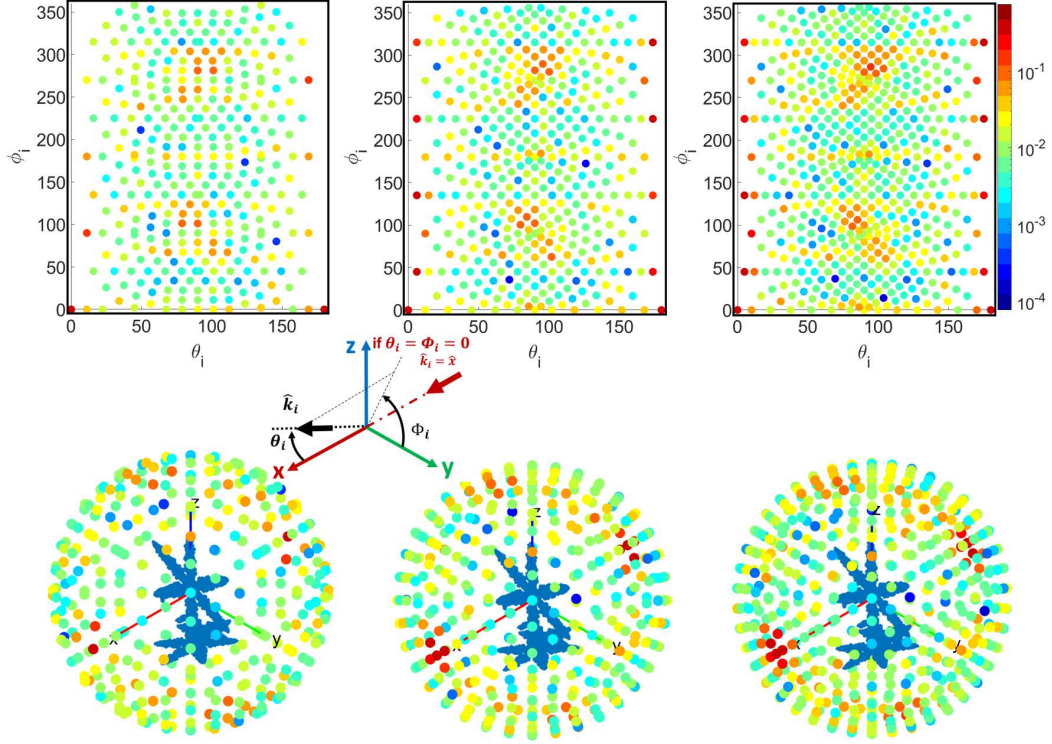


Figure 13: Backscatter efficiency Q_{bks} of a0012, using MIDAS with the lb scheme at $f = 94$ GHz, as function of the incident wave direction (θ_i, ϕ_i) . (top) 2D scatter plot (bottom) 3D visualization showing the impact of the particle shape on Q_{bks} over the sphere surface, along with the incident direction k_i defined by (θ_i, ϕ_i) . From left to right : Q_{bks} is calculated for 350, 434 and 590 IDs resulting in a relative difference E_r (%) in \overline{Q}_{bks} of -2.43% , 0.02% and 0.4% respectively..

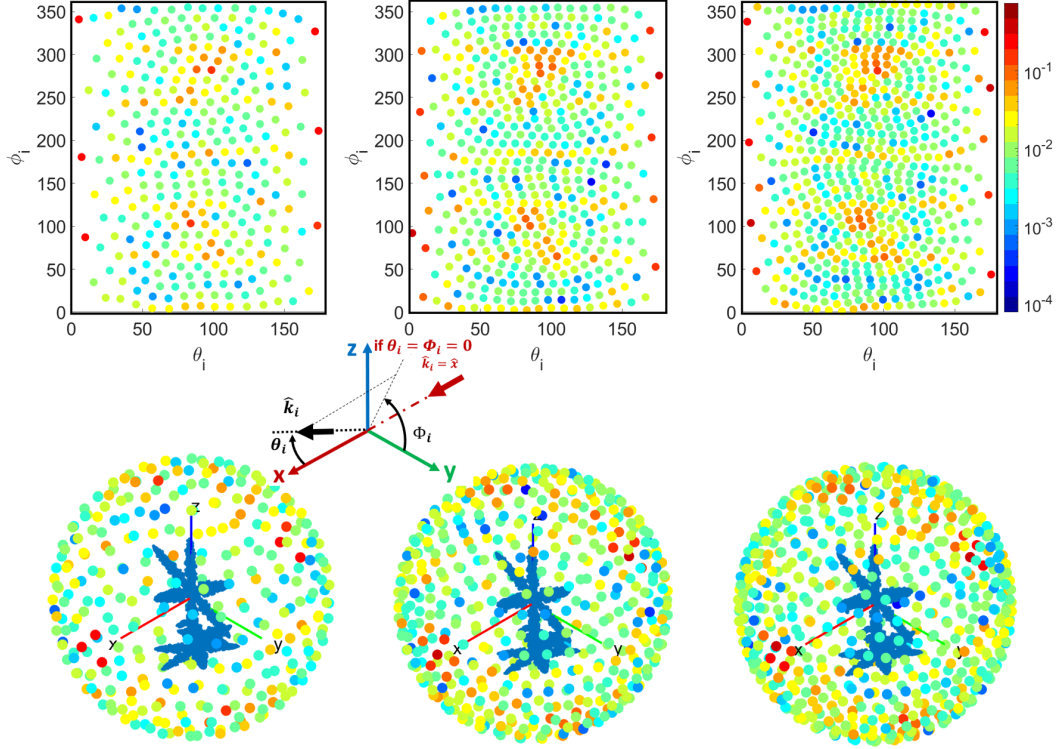


Figure 14: Backscatter efficiency Q_{bks} of a0012, using MIDAS with the sd scheme at $f = 94$ GHz, as function of the incident wave direction (θ_i, ϕ_i) . (top) 2D scatter plot (bottom) 3D visualization showing the impact of the particle shape on Q_{bks} over the sphere surface, along with the incident direction k_i defined by (θ_i, ϕ_i) . From left to right : Q_{bks} is calculated for 314, 482 and 614 IDs resulting in a relative difference E_r (%) in \overline{Q}_{bks} of 0.64%, 0.86% and 0.43% respectively.

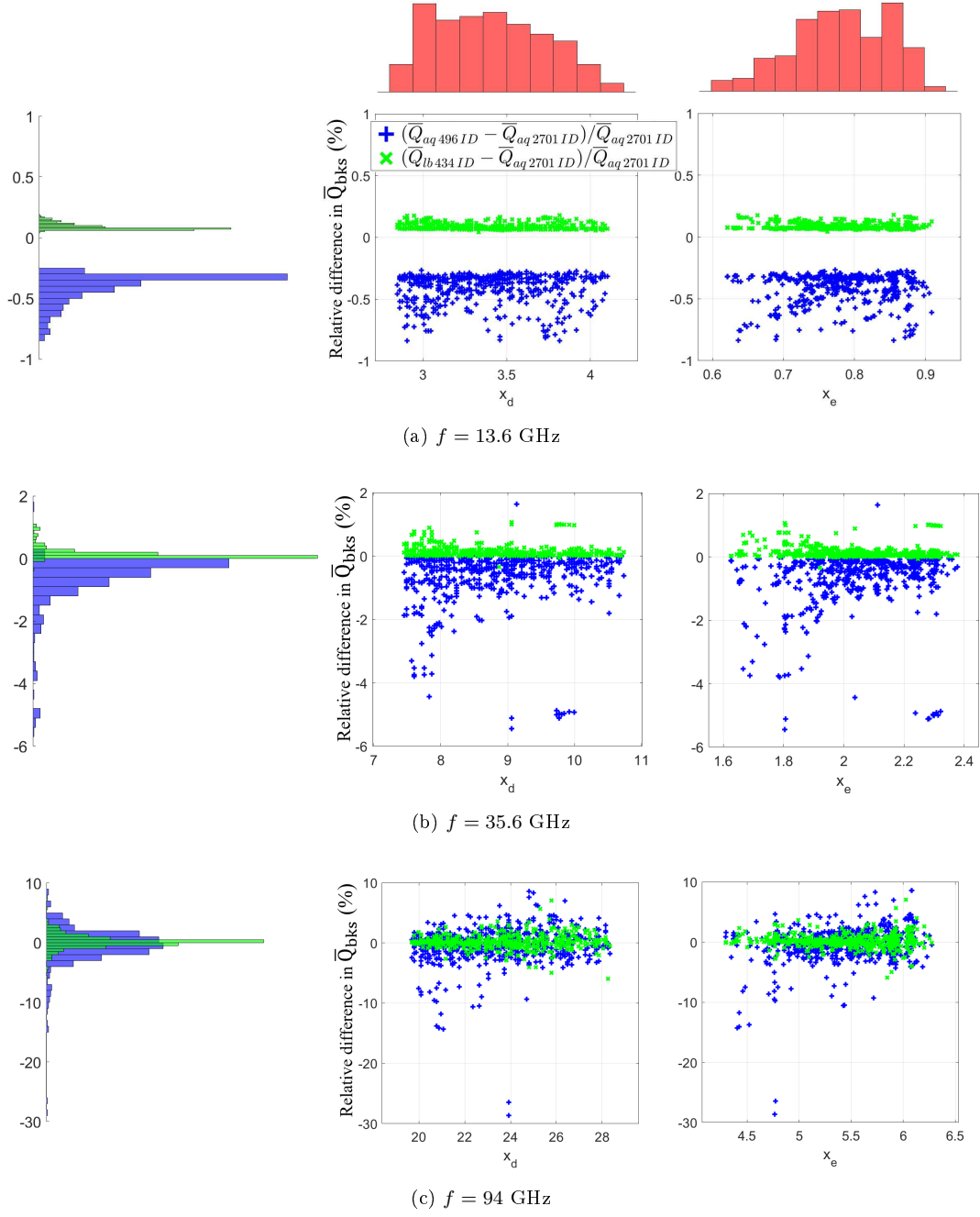


Figure 15: Variations of the relative difference in \overline{Q}_{bks} using MIDAS, with respect \overline{Q}_{bks} (2701 IDs), assumed to represent convergence, as function of x_d (middle) and x_e (right) when \overline{Q}_{bks} is calculated at Ku, Ka and W bands using aq with 496 IDs and lb with 434 IDs. The first column compares the distribution of Er (%) for aq with 496 IDs and lb with 434 IDs and the first row shows the distribution of x_d and x_e of the aggregates.

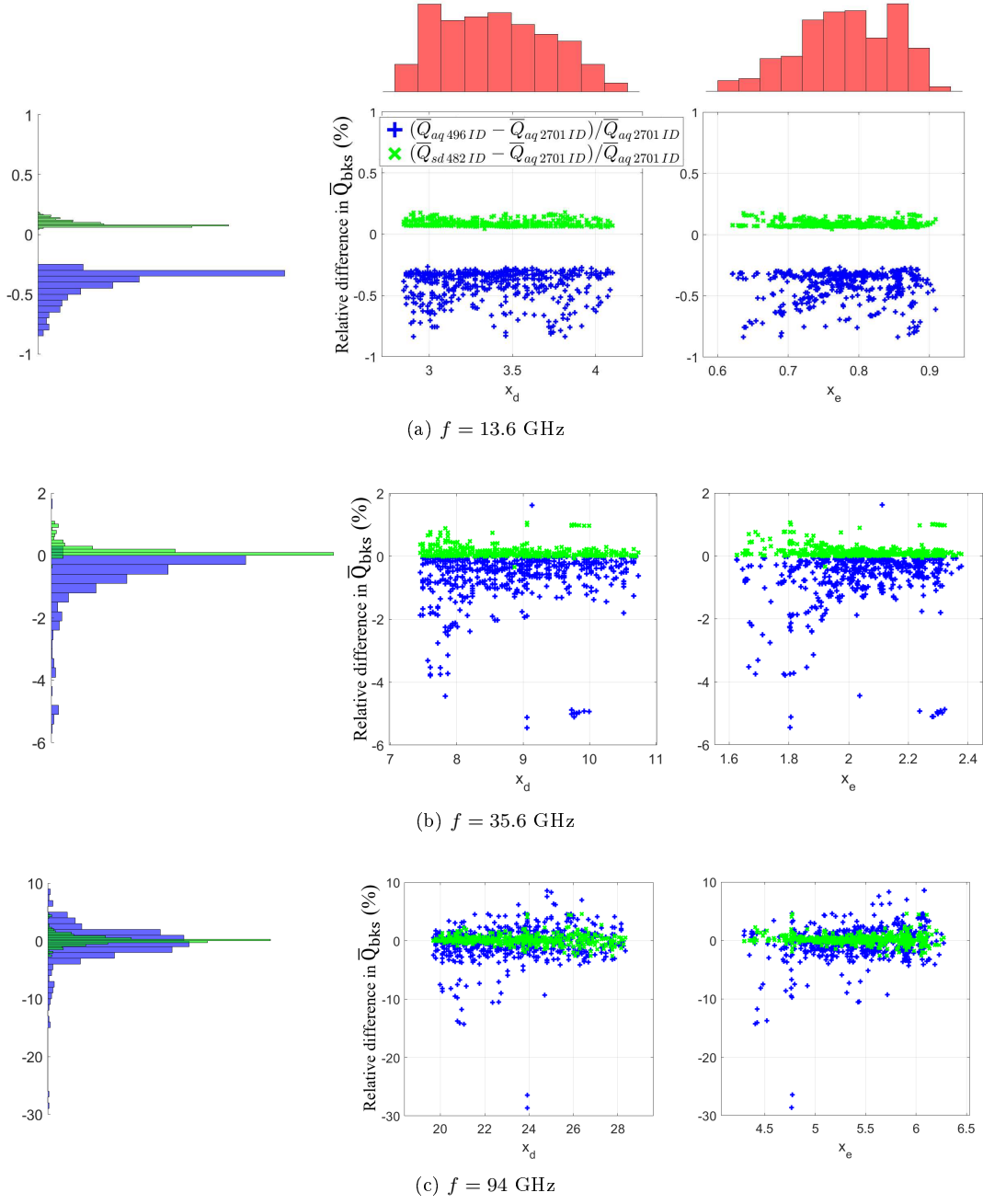


Figure 16: Variations of the relative difference in \bar{Q}_{bks} using MIDAS, with respect \bar{Q}_{bks} (2701 IDs), assumed to represent convergence, as function of x_d (middle) and x_e (right) when \bar{Q}_{bks} is calculated at Ku, Ka and W bands using aq with 496 IDs and sd with 482 IDs. The first column compares the distribution of Er (%) for aq with 496 IDs and sd with 482 IDs and the first row shows the distribution of x_d and x_e of the aggregates.

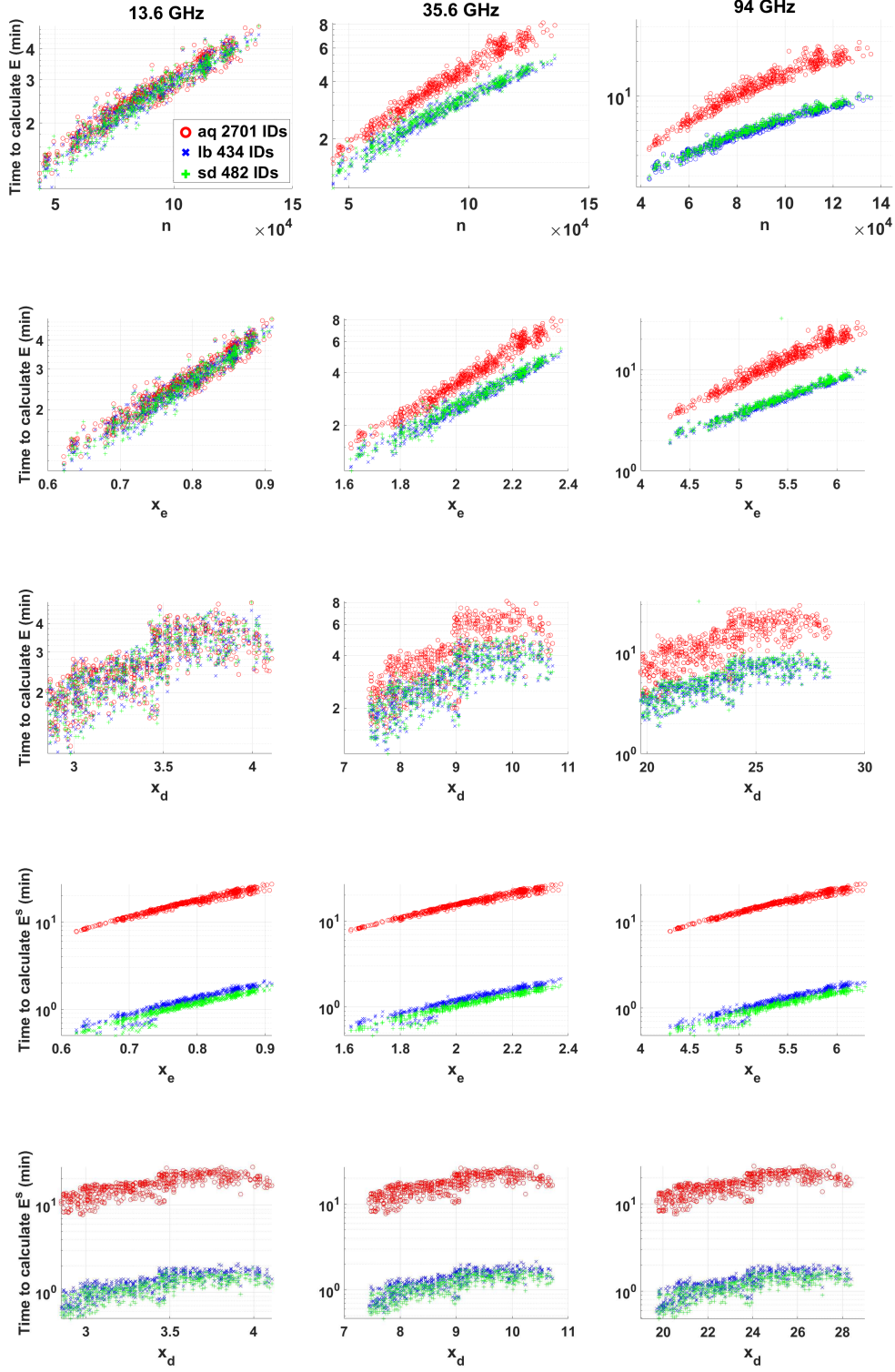


Figure 17: Computing time required at Ku, Ka and W bands to compute, using aq with 2701 IDs (reference simulation), lb with 434 IDs and sd with 482 IDs, the total electric field inside the snow aggregates \mathbf{E} (three top plots) as function of n the number of cells comprising the particle, x_e and x_d , and to compute the scattered field \mathbf{E}^s (two bottom plots) as function of x_e and x_d .

Acknowledgments

The research was mostly carried out at the Jet Propulsion Laboratory, California Institute of Technology, and University of Maryland, under a contract with the National Aeronautics and Space Administration (80NM0018D0004) within the Precipitation Measurement Missions Science Team (PMMST) program.

References

- Beentjes, C. H. (2015). Quadrature on a spherical surface. *Working note available on the website <http://people.maths.ox.ac.uk/beentjes/Essays>*.
- Bohren, C. F., & Singham, S. B. (1991). Backscattering by nonspherical particles: A review of methods and suggested new approaches. *Journal of Geophysical Research: Atmospheres*, 96(D3), 5269–5277.
- Burkardt, J. (2010a, February). *Sphere design rule hardin and sloane spherical designs*. Retrieved from https://people.sc.fsu.edu/~jburkardt/f_src/sphere_design_rule/sphere_design_rule.html (Accessed: 2020-02-03)
- Burkardt, J. (2010b, September). *Sphere lebedev rule quadrature rules for the unit sphere*. Retrieved from https://people.sc.fsu.edu/~jburkardt/f_src/sphere_lebedev_rule/sphere_lebedev_rule.html (Accessed: 2020-02-03)
- Deeter, M. N., & Evans, K. F. (1998). A hybrid eddington-single scattering radiative transfer model for computing radiances from thermally emitting atmospheres. *Journal of Quantitative Spectroscopy and Radiative Transfer*, 60(4), 635–648.
- Ding, J., Yang, P., Holz, R. E., Platnick, S., Meyer, K. G., Vaughan, M. A., . . . King, M. D. (2016). Ice cloud backscatter study and comparison with calipso and modis satellite data. *Optics Express*, 24(1), 620–636.
- Draine, B. T. (1988). The discrete-dipole approximation and its application to interstellar graphite grains. *The Astrophysical Journal*, 333, 848–872.
- Draine, B. T., & Flatau, P. J. (1994). Discrete-dipole approximation for scattering calculations. *JOSA A*, 11(4), 1491–1499.
- Draine, B. T., & Flatau, P. J. (2013). User guide for the discrete dipole approximation code ddscat 7.3.
- Eriksson, P., Ekelund, R., Mendrok, J., Brath, M., Lemke, O., & Buehler, S. A. (2018). A general database of hydrometeor single scattering properties at microwave and sub-millimetre wavelengths. *Earth System Science Data*, 10(3), 1301–1326.
- Evans, K. F., & Stephens, G. L. (1995). Microwave radiative transfer through clouds composed of realistically shaped ice crystals. part ii. remote sensing of ice clouds. *Journal of the Atmospheric Sciences*, 52(11), 2058–2072.
- Fenni, I., Haddad, Z. S., Roussel, H., Kuo, K. S., & Mittra, R. (2018). A computationally efficient 3-d full-wave model for coherent em scattering from complex-geometry hydrometeors based on mom/cbfm-enhanced algorithm. *IEEE Transactions on Geoscience and Remote Sensing*, 56(5), 2674–2688.
- Fenni, I., Roussel, H., Darces, M., & Mittra, R. (2016, Oct). Efficiency enhancement of the characteristic basis function method for modeling forest scattering using the adaptive cross approximation algorithm. *IEEE Transactions on Antennas and Propagation*, 64(10), 4539–4544.
- Gravner, J., & Griffeath, D. (2009). Modeling snow-crystal growth: A three-dimensional mesoscopic approach. *Physical Review E*, 79(1), 011601.
- Haddad, Z. S., Smith, E. A., Kummerow, C. D., Iguchi, T., Farrar, M. R., Durden, S. L., . . . Olson, W. S. (1997). The trmm 'day-1' radar/radiometer combined rain-profiling algorithm. *Journal of the Meteorological Society of Japan. Ser. II*, 75(4), 799–809.
- Haddad, Z. S., Sy, O. O., Hristova-Veleva, S., & Stephens, G. L. (2017). Derived observations from frequently sampled microwave measurements of precipitation—part i: Relations to atmospheric thermodynamics. *IEEE Transactions on Geoscience and Remote Sensing*, 55(6), 3441–3453.

- Hardin, R. H., & Sloane, N. J. (1996). McLaren's improved snub cube and other new spherical designs in three dimensions. *Discrete & Computational Geometry*, 15(4), 429–441.
- Hou, A. Y., Kakar, R. K., Neeck, S., Azarbarzin, A. A., Kummerow, C. D., Kojima, M., ... Iguchi, T. (2014). The global precipitation measurement mission. *Bulletin of the American Meteorological Society*, 95(5), 701–722.
- Johnson, B. T., Olson, W. S., & Skofronick-Jackson, G. (2015). The microwave properties of simulated melting precipitation particles: sensitivity to initial melting. *Atmospheric Measurement Techniques Discussions*, 8(6).
- Kneifel, S., Dias Neto, J., Ori, D., Moiseev, D., Tyynelä, J., Adams, I. S., ... others (2018). Summer snowfall workshop: Scattering properties of realistic frozen hydrometeors from simulations and observations, as well as defining a new standard for scattering databases. *Bulletin of the American Meteorological Society*, 99(3), ES55–ES58.
- Kummerow, C., Barnes, W., Kozu, T., Shiue, J., & Simpson, J. (1998). The tropical rainfall measuring mission (trmm) sensor package. *Journal of atmospheric and oceanic technology*, 15(3), 809–817.
- Kummerow, C., Simpson, J., Thiele, O., Barnes, W., Chang, A., Stocker, E., ... others (2000). The status of the tropical rainfall measuring mission (trmm) after two years in orbit. *Journal of applied meteorology*, 39(12), 1965–1982.
- Kuo, K.-S., Olson, W. S., Johnson, B. T., Grecu, M., Tian, L., Clune, T. L., ... Meneghini, R. (2016). The microwave radiative properties of falling snow derived from nonspherical ice particle models. part i: An extensive database of simulated pristine crystals and aggregate particles, and their scattering properties. *Journal of Applied Meteorology and Climatology*, 55(3), 691–708.
- Liu, G. (2008). A database of microwave single-scattering properties for nonspherical ice particles. *Bulletin of the American Meteorological Society*, 89(10), 1563–1570.
- Lu, Y., Jiang, Z., Aydin, K., Verlinde, J., Clothiaux, E. E., & Botta, G. (2016). A polarimetric scattering database for non-spherical ice particles at microwave wavelengths. *Atmospheric Measurement Techniques*, 9(10), 5119–5134.
- Lucente, E., Monorchio, A., & Mittra, R. (2008). An iteration-free mom approach based on excitation independent characteristic basis functions for solving large multiscale electromagnetic scattering problems. *Antennas and Propagation, IEEE Transactions on*, 56(4), 999–1007.
- Mishchenko, M. I. (2014). *Electromagnetic scattering by particles and particle groups: an introduction*. Cambridge University Press.
- Mittra, R., & Du, K. (2008). Characteristic basis function method for iteration-free solution of large method of moments problems. *Progress In Electromagnetics Research B*, 6, 307–336.
- Munchak, S. J. (2018). Remote sensing of precipitation from airborne and spaceborne radar. In *Remote sensing of aerosols, clouds, and precipitation* (pp. 267–299). Elsevier.
- Nowell, H., Liu, G., & Honeyager, R. (2013). Modeling the microwave single-scattering properties of aggregate snowflakes. *Journal of Geophysical Research: Atmospheres*, 118(14), 7873–7885.
- Okada, Y. (2008). Efficient numerical orientation averaging of light scattering properties with a quasi-monte-carlo method. *Journal of Quantitative Spectroscopy and Radiative Transfer*, 109(9), 1719–1742.
- Olson, W. S., Tian, L., Grecu, M., Kuo, K.-S., Johnson, B. T., Heymsfield, A. J., ... Meneghini, R. (2016). The microwave radiative properties of falling snow derived from nonspherical ice particle models. part ii: Initial testing using radar, radiometer and in situ observations. *Journal of Applied Meteorology and Climatology*, 55(3), 709–722.
- Ori, D., Maestri, T., Rizzi, R., Cimini, D., Montopoli, M., & Marzano, F. (2014). Scattering properties of modeled complex snowflakes and mixed-phase particles at microwave and millimeter frequencies. *Journal of Geophysical Research: Atmospheres*, 119(16), 9931–9947.

- 813 Penttilä, A., & Lumme, K. (2011). Optimal cubature on the sphere and other orienta-
 814 tion averaging schemes. *Journal of Quantitative Spectroscopy and Radiative Transfer*,
 815 112(11), 1741–1746.
- 816 Penttilä, A., Zubko, E., Lumme, K., Muinonen, K., Yurkin, M. A., Draine, B., ... Shku-
 817 ratov, Y. (2007). Comparison between discrete dipole implementations and exact
 818 techniques. *Journal of Quantitative Spectroscopy and Radiative Transfer*, 106(1),
 819 417–436.
- 820 Petty, G. W., & Huang, W. (2010). Microwave backscatter and extinction by soft ice spheres
 821 and complex snow aggregates. *Journal of the Atmospheric Sciences*, 67(3), 769–787.
- 822 Piessens, R., de Doncker-Kapenga, E., Überhuber, C. W., & Kahaner, D. K. (1983). *Quad-*
 823 *pack: a subroutine package for automatic integration* (Vol. 1). Springer Science &
 824 Business Media.
- 825 Purcell, E. M., & Pennypacker, C. R. (1973). Scattering and absorption of light by non-
 826 spherical dielectric grains. *The Astrophysical Journal*, 186, 705–714.
- 827 Stephens, G. L., Vane, D. G., Boain, R. J., Mace, G. G., Sassen, K., Wang, Z., ... others
 828 (2002). The cloudsat mission and the a-train: A new dimension of space-based obser-
 829 vations of clouds and precipitation. *Bulletin of the American Meteorological Society*,
 830 83(12), 1771–1790.
- 831 Stephens, G. L., Vane, D. G., Tanelli, S., Im, E., Durden, S., Rokey, M., ... others (2008).
 832 Cloudsat mission: Performance and early science after the first year of operation.
 833 *Journal of Geophysical Research: Atmospheres*, 113(D8).
- 834 Um, J., & McFarquhar, G. M. (2013). Optimal numerical methods for determining the
 835 orientation averages of single-scattering properties of atmospheric ice crystals. *Journal*
 836 *of Quantitative Spectroscopy and Radiative Transfer*, 127, 207–223.
- 837 Warren, S. G. (1984). Optical constants of ice from the ultraviolet to the microwave. *Applied*
 838 *optics*, 23(8), 1206–1225.
- 839 Womersley, R. (2017, February). *Efficient spherical designs with good geometric properties*.
 840 <https://web.maths.unsw.edu.au/~rsw/Sphere/EffSphDes/>. (Accessed: 2020-02-
 841 03)
- 842 Womersley, R. S. (2018). Efficient spherical designs with good geometric properties. In
 843 *Contemporary computational mathematics-a celebration of the 80th birthday of ian*
 844 *sloan* (pp. 1243–1285). Springer.
- 845 Yaghjian, A. D. (1996). Sampling criteria for resonant antennas and scatterers. *Journal of*
 846 *applied physics*, 79(10), 7474–7482.
- 847 Yurkin, M. A., & Hoekstra, A. G. (2007). The discrete dipole approximation: an overview
 848 and recent developments. *Journal of Quantitative Spectroscopy and Radiative Trans-*
 849 *fer*, 106(1), 558–589.
- 850 Yurkin, M. A., & Hoekstra, A. G. (2011). The discrete-dipole-approximation code adda:
 851 capabilities and known limitations. *Journal of Quantitative Spectroscopy and Radiative*
 852 *Transfer*, 112(13), 2234–2247.